



1

2

3 Peer review status:

4 This is a non-peer-reviewed preprint submission to EarthArXiv

5

6

7

8 Smoothing Earth's surface: the complexity of soil 9 texture class transitions

10 *Trevan Flynn^{*1}, Zahra Rasaei², Rosana Kostecki^{3,4}*

11

12 ^{*1}Department of Agronomy, University of Forte Hare, Alice 5700 South Africa

13 ²Department of Soil Science, University of Tehran, Karaj 77871 Iran

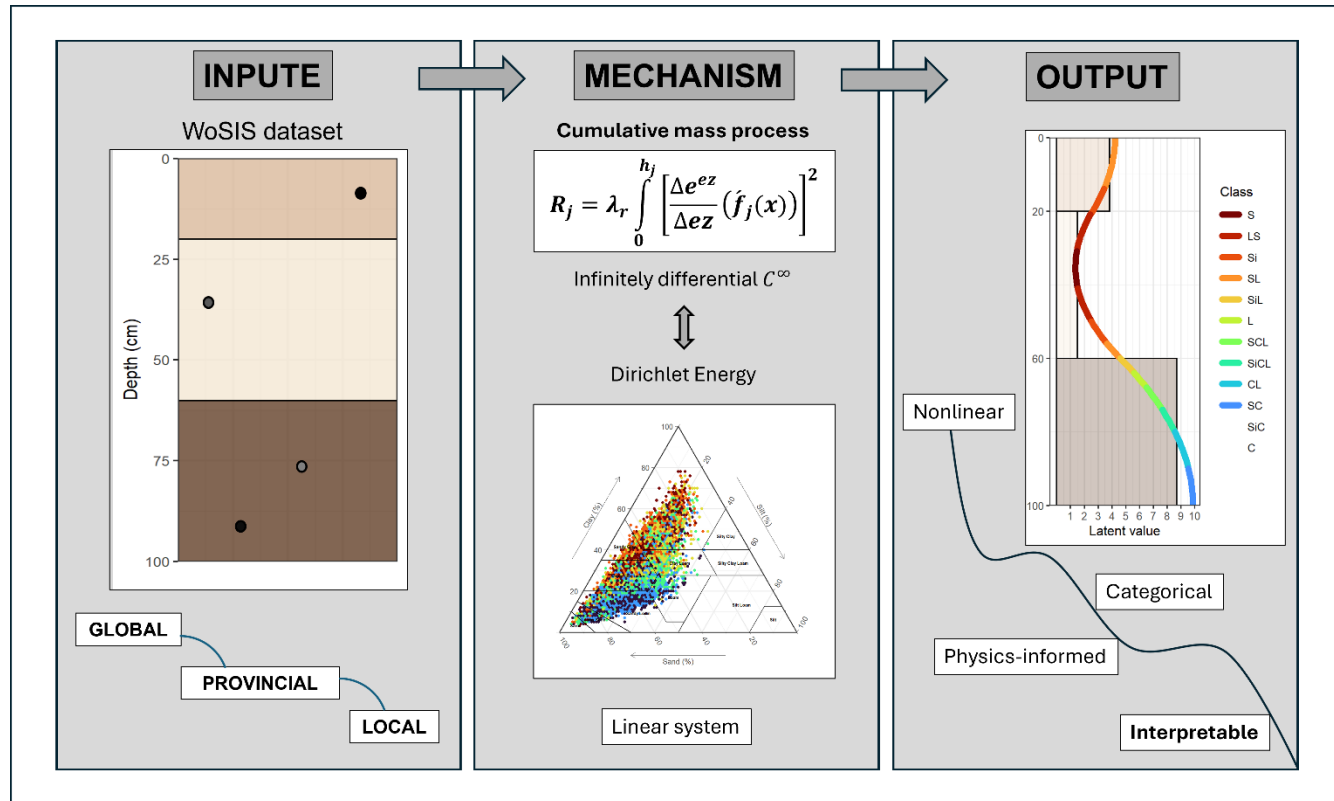
14 ³Soil Consultoria Socioambiental, R. Prof. Joaquim de Matos Barreto, 88-Lima Azevedo, Londrina
15 86015 Brasil

16 ⁴Department of Geography, State University of Londrina, Londrina 86055 Brasil

17

18 *Corresponding author email: trevanflynn@gmail.com

19



20

21 **Abstract**

22 Soil depth functions are essential for analysing, modeling, understanding and visualising soil profiles.

23 While robust methods existed for continuous properties, soil texture is typically reported as discrete

24 classes, and no established approach exists to interpolate soil categorical information with depth. Here,

25 we introduced phySplines, a physics-informed, analytically solvable spline for interpolating soil

26 categorical information. Soil texture classes were mapped to a latent numerical space and continuously

27 interpolated by minimising the depth-weighted Dirichlet energy via the exact analytic integral of Euler's

28 cumulative mass process, which encoded depth-dependent resistance and enforces non-parametric

29 physically consistent smoothness. PhySplines achieved kappa values of 0.96, 0.94 and 0.96 at global,

30 provincial and local scales, respectively. By embedding pedological theory within a fully continuous and

31 interpolation framework, the function avoided over representation of dominant classes, captured

32 previously unmodelled transitional states, mitigated the drift effect and generalised across missing layers.

33 PhySplines maintained mass and energy continuity (infinitely differentiable C^∞) without over-

34 constraining the solution, allowing for greater flexibility for future work into numerical classification

35 and the quantification of soil thermodynamical multifunctionality. Ultimately, minimising potential

36 energy and maintaining the mass continuity, phySplines transformed complex soil profiles into

37 dynamic, interpretable narratives, allowing users to "see" between horizons.

38 **Keywords:** Exact analytic integral; Depth function; Dirichlet Energy; Infinite Differentiability; Physics-
39 informed

41 1 Introduction

42 Interpolation of properties with depth is a common practice across many scientific disciplines (Ma et al.,
43 2026; Odom and Doctor, 2023; Probst et al., 2018; Rogozovsky et al., 2025; Zhao et al., 2025) and has
44 become standard in soil analysis (Amundson et al., 2025; Benbi and Toor, 2026; Pei et al., 2025; Souza
45 et al., 2023). Depth functions expand datasets by enabling harmonisation with other datasets (Cheng et
46 al., 2024), improve understanding of soil profile physical (Zhang et al., 2023) and biochemical dynamics
47 (Leewis et al., 2022) and support downstream applications in hydrology, ecology and environmental
48 management (Ruiz et al., 2025). By providing representations that are mathematically robust yet easy to
49 conceptualise and visualise, depth functions help facilitate communication with scientists, policymakers
50 and communities.

51 Several approaches exist for representing soil properties with depth, including exponential decay
52 (Kempen et al., 2011; Wiese et al., 2016), polynomials (Colwell, 1970; Russell and Moore, 1968), cubic
53 splines (Flynn et al., 2022b), equal-area splines (ea-splines) (Bishop et al., 1999; Malone et al., 2009;
54 Ponce-Hernandez et al., 1986) and grid-based ea-splines (Flynn et al., 2024). Unlike standard smoothing
55 splines, ea-splines are formulated such that the integral of the spline equals the observed horizon mean,
56 ensuring mass preservation with each horizon (Bishop et al., 1999; Ponce-Hernandez et al., 1986).
57 Despite the benefits of continuous depth functions, limited soil profile observations may over-constrain
58 them, leading to unrealistic values and increased criticism (Kienast-Brown et al., 2021).

59 Nevertheless, soil depth functions have rarely accommodated categorical data such as soil texture classes,
60 which carry critical information for farmers, educators and land managers. The historical absence of
61 robust methods for interpolating categorical data arises from the misconception that discrete soil classes
62 do not exhibit boundary or transitional behavior (Burrough et al., 1997; Henderson et al., 2025) and partly
63 from the inherent complexity of categorical mathematics (Basu and Isik, 2020; Yanofsky, 2015).
64 Furthermore, traditional taxonomic dissemination tools are rarely designed for numerical modeling

65 (Zhang and Goodchild, 2002), creating bottlenecks that lead to information loss, computational
66 inefficiency and a disconnect between soil taxonomy and the quantitative requirements of environmental
67 models (Bortolus, 2008; Hillebrand et al., 2018; Isaac, 2004; Weiskopf et al., 2022).

68 The aim of this study was to develop phySplines, a physics-informed, analytically solvable spline for
69 interpolating categorical soil information to standardised depths across global, provincial and local
70 scales. Specifically, we sought to: (i) develop fully continuous, differentiable and mass-preserving
71 categorical splines that maintain pedological realism across spatial supports; (ii) incorporate physics-
72 informed constraints into an analytically solvable formulation, providing insight into class behaviour
73 while remaining computationally scalable without over-constraining; and (iii) develop a deterministic
74 spline capable of predicting “unseen” categories and inferring transitional or boundary classes suggested
75 by depth gradients, even when such classes were not directly observed in the profile. These innovations
76 introduce pedological realism by enforcing continuous, process-based gradients and transitions,
77 effectively bridging taxonomic information with the rigorous requirements of numerical environmental
78 modeling.

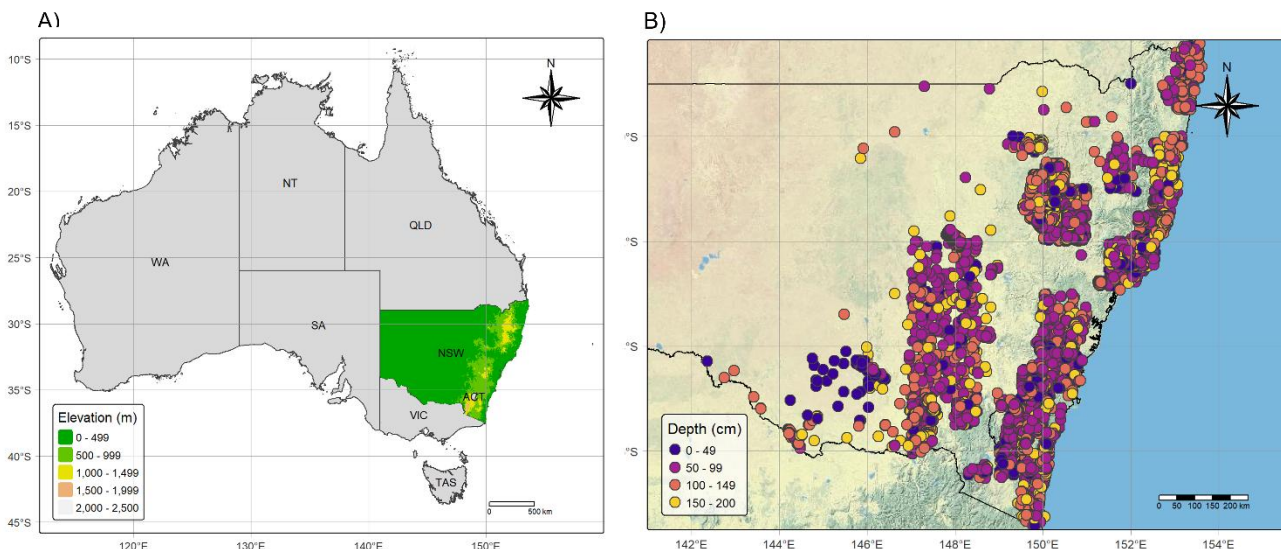
79 2 Methods and materials

80 2.1 Soil observations

81 To evaluate whether phySplines can be applied globally, across different spatial supports and for various
82 purposes, the spline was tested at three spatial scales. Data was obtained from the World Soil Information
83 Systems (WoSIS) dataset (ISRIC, 2021), which provides nearly global coverage. The global scale
84 encompassed most of the soil forming factors as well as soil functions that contribute to society and the
85 environment. Observations were included for analysis if they had United States Department of
86 Agriculture (USDA) soil texture classes assigned or had clay, silt and sand fractions summing to 100%
87 and the soil depth was ≤ 200 cm. A depth limit of 200 cm was applied because most international and

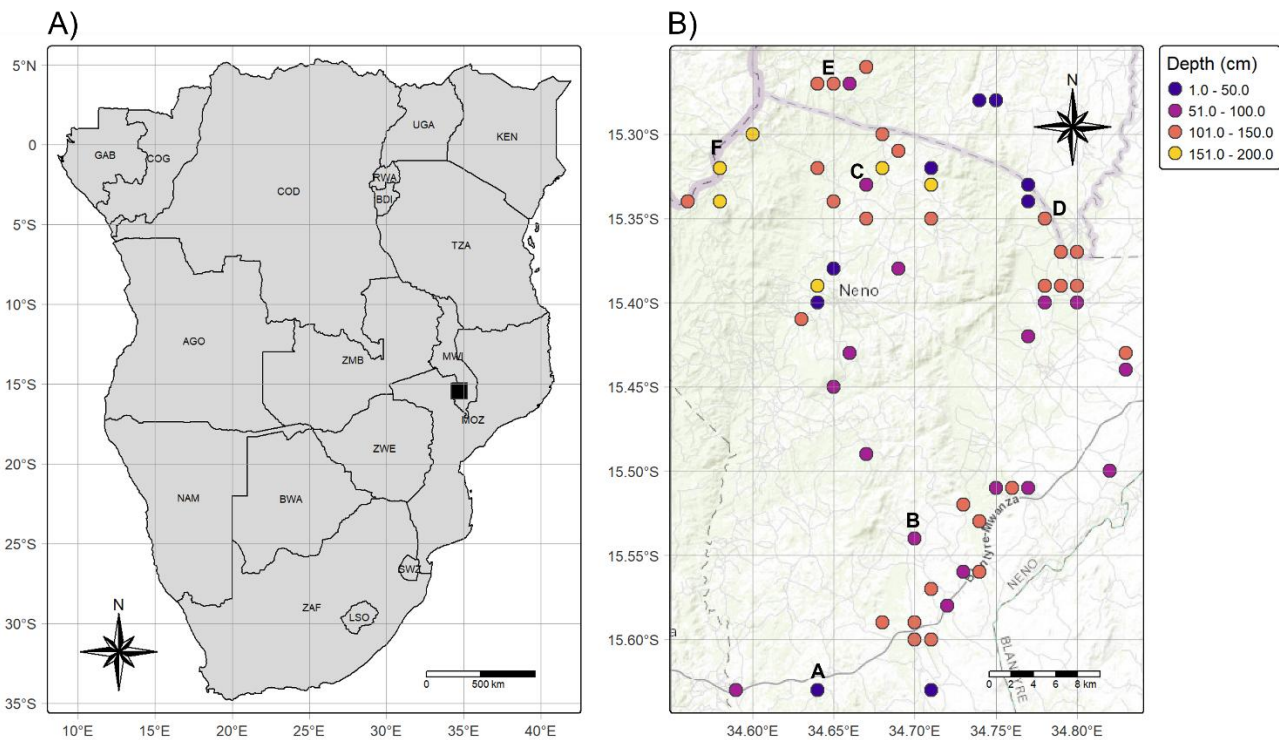
88 national soil classification systems, including the World Reference Base (WRB) and USDA Soil
89 Taxonomy, do not define diagnostic criteria beyond this depth. After filtering, a total of 101,568 soil
90 observations were retained for global analysis with or without missing horizons.

91 The WoSIS dataset included 6,791 observations (0.008 samples km⁻²) at the provincial scale across New
92 South Wales (NSW), Australia (Figure 1), covering approximately 801,150 km² (center ≈147°1'E to
93 32°9'S). Elevation ranges from sea level to >2,000 m in the southeastern highlands. The geology is unique
94 with distinct sedimentary basins, with widespread sodic soil formed during episodes of landscape uplift
95 (Blewett, 2012). Climate and vegetation are highly variable across the province (Australian Bureau Of
96 Meteorology, 2019) with both winter and summer cropping systems represented (McDougall et al., 2002;
97 NSW Department of Primary Industries, 2020). Major urban centres are concentrated along the coast,
98 whereas inland areas are predominantly rural and agriculturally oriented (Smith and Robert B.
99 Thompson, 2019). The province was selected because it is among the most extensively studied regions
100 in quantitative pedology (e.g., the Hunter Valley), nearly all available profiles met the study criteria
101 (<200 cm depth and particle-size fractions summing to 100%) and the province encompasses a broad
102 range of environmental conditions relevant to pedogenesis.



103
104 *Figure 1: The elevation of New South Wales (NSW) within Australia (A) and the soil observations with depth of NSW (B).*

105 A region in southern Malawi (center $\approx 34^{\circ}41'42''E$, $15^{\circ}26'42''S$) was selected to evaluate phySplines at
 106 the local scale due to the relatively high number of WoSIS soil observations (0.05 samples km^{-2}) within
 107 a $1,191$ km^2 area (Figure 2). Located northwest of Blantyre in the Neno District, there were 65 profiles
 108 within and around a valley to the Lisungwe River, which drains to the Shire River, the primary outlet of
 109 Lake Malawi. The elevation ranges from 256 to 1,635 m, corresponding to strong gradients in mean
 110 annual temperature and precipitation (Fick and Hijmans, 2017). The region has a subtropical Udic soil
 111 moisture regime and is dominated by smallholder agriculture, including tobacco, cotton, maize, soybean
 112 and groundnut production (Araya et al., 2023). This site was selected because it provides sufficient profile
 113 density to evaluate local-scale model behaviour and represents an environmentally sensitive landscape
 114 relevant to soil–water and land-use management.



115

116 *Figure 2: Neno District (not to scale), Malawi within southern Africa (A) and the soil samples with depth within Neno District (B).*
 117 Cross-scale validation was used to explicitly test the sensitivity of phySpline to observation density and
 118 spatial heterogeneity. The global dataset spans highly variable soil environments with uneven sampling

119 densities, the NSW dataset represents a spatially biased setting with moderate observational support, and
120 the Neno dataset reflects a dense but spatially constrained context. Consistent performance across these
121 scales indicates that phySpline does not depend on scale-specific tuning or regional calibration, but
122 instead derives stability from its physically constrained formulation.

123 For all scales, USDA soil texture classes comprised 12 categories, derived from clay, silt, and sand
124 fractions on a texture triangle. The natural ordinal rank, from sand (1) to clay (1), was used for the
125 physical process representing particle mass and surface area from the smallest to largest; the data was
126 treated as unranked ordinal. Table 1 summarises the class symbols, names, latent value and the number
127 of observations at the global, provincial and local scales.

128 *Table 1: The United States Department of Agriculture (USDA) soil texture class symbol, name, latent value (Order) and the*
129 *number of observations (n) for the global, provincial and local scales.*

Class	Name	Order	Global (n)	Provincial (n)	Local (n)
S	Sand	1	28,390	824	3
LS	Loamy sand	2	28,511	1,400	50
Si	Silt	3	1,983	3	0
SL	Sandy loam	4	77,663	3,869	60
SiL	Silty loam	5	70,733	83	0
L	Loam	6	60,196	943	1
SCL	Sandy clay loam	7	35,856	4,024	56
SiCL	Silty clay loam	8	40,116	47	0
CL	Clay loam	9	35,977	1102	0
SC	Sandy clay	10	10,394	1,184	30
SiC	Silty clay	11	22,543	57	0
C	Clay	12	67,364	9,044	12

130

131 2.2 PhySpline theory

132 PhySplines are an energy-minimising function fitted through an exact integral function derived from
133 classical mechanics. Along with the conservation of mass, the spline is based on potential energy, where
134 the curve adjusts to maintain minimal energy through the cumulative mass of the soil column and
135 boundary conditions with the surface, lithosphere and hydrosphere. In this case, we imposed a
136 mathematical steady state by enforcing a zero flux and a geogenic steady state for the top and bottom
137 horizons, respectively. Therefore, along with mass conservation, we enforce mass and energy continuity
138 in a fully continuous, non-parametric function and move away from geometric midpoints toward the
139 exact integral of the minimised energy.

140 2.2.1 Fundamental concept

141 To enable the use of categorical soil data, discrete soil texture classes were first mapped onto an ordered
142 latent numerical axis by class symbols with order (Table 1). This ordinal transformation preserves the
143 natural progression of texture from coarse to fine, allowing interpolation in continuous space while
144 retaining categorical interpretability. Although soil texture triangles are conventionally defined by sand,
145 silt and clay, the latent mapping flattened this multi-dimensional space into a one-dimensional sequence,
146 with sand and clay as the endmembers. This simplification converts the complex multi-dimensional
147 problem into a standard depth function, facilitating spline interpolation and process-based interpretation.
148 This approach assumes that soil texture classes can be treated as ordinal data.

149 Each spline segment self-regularises, stiffening naturally with cumulative horizon mass according to an
150 exponential process Euler's (e) cumulative mass process, effectively following a steady-state definite
151 integral that limits unrealistic slopes. Latent values were then mapped to the nearest soil texture classes
152 to produce harmonised, physically consistent profiles. Profile harmonisation was achieved by integrating
153 the fitted latent values to the GlobalSoilMap standard depth intervals (0–5, 5–15, 15–30, 30–60, 60–100

154 and 100–200 cm). The harmonised dataset, source code, and the rafikisol R package (Flynn, 2023) are
155 available at www.github.com/rafikisol/rafikisol.

156 Key components of the phySpline formulation include:

- 157 • Continuous data fidelity: Observations contribute through a fully continuous loss function,
158 integrating across horizon thicknesses rather than relying on geometric midpoints.
- 159 • Definite integral: The spline was coefficients were estimated using the exact integral for the
160 entire profile, being infinite differentiable C^∞ .
- 161 • Boundary conditions: The constraint matrix anchored the slope at the top and bottom, ensuring
162 the profile naturally returned to vertical at the boundaries.
- 163 • Physics-informed regularisation: The splines curve is dependent on the cumulative mass above
164 in a continuous manner from the Euler’s cumulative mass process.
- 165 • Explicit matrix formulation: The design matrix A , regularisation matrix R and Jacobian
166 constraint matrix G are fully specified, enabling direct and transparent control over constraint
167 enforcement.
- 168 • Inter-horizon continuity: Continuity of both values (C^0) and first derivatives (C^1) are enforced
169 across horizon boundaries via a null-space projection of G , ensuring physically informed
170 constraints are satisfied exactly.
- 171 • Latent class preservation: Continuous latent values are mapped back to discrete soil texture
172 classes, maintaining interpretability while enabling continuous interpolation.

173 These central concepts of the phySpline go along with the paradigm shift in depth functions as we move
174 away from functions that produce unrealistic estimates. However, instead of using the point depth approach like
175 the USDA digital soil mapping focus team (Kienast-Brown et al., 2021); we decided to make sure the
176 spline was pedologically realistic, not over-constrained and obeyed physical laws.

177 2.2.2 Potential energy of soil

178 In phySplines, the soil profile is represented as a one-dimensional scalar field evolving within a potential-
 179 energy framework, where profile smoothness corresponds to the energetic cost of deformation. Since
 180 potential energy is defined through spatial gradients, this formulation aligns with pedological theory, in
 181 which soil profiles result from gravity-driven transport, diffusion and kinetically limited processes acting
 182 over depth and time (Hillel, 1998). This framework is not limited to pedology but is applicable across
 183 scientific disciplines, where potential energy provide the thermodynamic basis of soil multifunctionality
 184 and the capacity of soils to deliver ecosystem services (Kleidon, 2010). Therefore, this is not a random
 185 physics-informed theory, but one that is pedologically relevant and connects across disciplines,
 186 enhancing communication.

187 Within this framework, the soil profile is modeled as a scalar field $f(z)$ embedded in a heterogeneous
 188 medium with a depth-dependent resistance function $D(z)$. Under steady-state conditions, the profile
 189 minimises a weighted Dirichlet energy and satisfies the Euler–Lagrange equation:

$$190 \quad \frac{d}{dz} \left(D(z) \frac{df(dz)}{dz} \right) = 0$$

191 with corresponding potential energy functional:

$$192 \quad E[f] = \frac{1}{2} \int_o^H D(z) \left(\frac{df}{dz} \right)^2 dz$$

193 Here, $D(z)$ represents the local energetic resistance to slope change, reflecting mechanical and structural
 194 constraints of deeper soil layers due to compaction, overburden, clay illuviation and reduced biological
 195 mixing. This formulation naturally permits greater flexibility near the surface while progressively
 196 constraining curvature at depth, producing smooth and physically consistent profiles.

197 To model the monotonic increase in resistance while retaining analytical tractability, $D(z)$ is expressed
198 as an exponential function:

199
$$D(z) = D_o e^{kz}$$

200 which arises from the assumption that resistance increases proportionally to its current magnitude. The
201 exponential form of the resistance function arises naturally as the solution to a first-order growth process,
202 where the rate of change in soil stiffness is proportional to its current magnitude. The parameter k
203 represents the attenuation coefficient of pedological influence, while z defines the latent taxonomic
204 intensity, providing a coordinate system where physical stability is linked directly to the soil's
205 developmental state. The inclusion of Euler's number e ensures that this increase in resistance with depth
206 is both continuous and scale-independent.

207 2.2.3 Physics-informed spline

208 The phySpline theory is expressed directly through the equations used in implementation, ensuring that
209 the mathematical formulation and computational realization are identical. The phySpline for each horizon
210 was expressed as a piecewise quadratic function:

211
$$f_j(x) = \alpha_j + b_j(x - u_j) + \gamma_j(x - u_j)^2,$$

212 where α_j is the value at the top of horizon j , b_j is the slope at the top of the horizon, γ_j controls the
213 curvature of the function within the horizon, and u_j is the top depth of horizon j . The curvature term γ_j
214 governs the redistribution of slope with depth, allowing internal deformation while maintaining
215 continuity at horizon boundaries. To estimate the coefficients $\beta = (\alpha_j, b_j, \gamma_j)$, data fidelity, regularisation
216 (roughness control), and inter-horizon continuity must be jointly enforced.

217 The data fidelity loss function was formulated as the continuous integral over each horizon to preserve
218 the exact mean, numerical stability and class structure.

219

$$L(A) = \frac{1}{2} ||y - A\beta||_2^2 = \frac{1}{n} \sum_{j=1}^n \left(\int_0^{h_j} f_j(x) dx - y_j \right)^2$$

220 where h_j is the thickness of horizon j and the integral measures the squared difference between the spline-
 221 interpolated values $f_j(x)$ and the observed values y_j .

222 For the regularization term, pedological theory governs the conceptual model, physics governs the
 223 horizons, with smoothness arising from the minimisation of potential energy within each horizon. Spline
 224 smoothness was governed by a depth-weighted Dirichlet energy defined through the exact analytic
 225 integral of a global Euler cumulative mass process. Rather than treating regularisation as a numerical
 226 penalty or imposing boundary conditions, the energetic cost of deformation was integrated over each
 227 horizon, allowing smoothness and curvature to emerge naturally from the profile itself. For horizon j ,
 228 the energy minimised was

229

$$R_j = \lambda_r \int_0^{h_j} \left[\frac{\Delta e^{ez_j}}{\Delta ez_j} [\hat{f}_j(x)] \right]^2 dx,$$

230 where $f_j(x)$ is the piecewise polynomial representing the profile, h_j is the horizon thickness, ez is the
 231 global normalised depth $z \in [0, 1]$. The exponential term represents a depth-dependent stiffness,
 232 reflecting increasing mechanical and structural resistance with depth, while the difference-quotient
 233 formulation evaluated resistance as a physically meaningful process that is infinitely differentiable C^∞ .
 234 Cumulative mass resistance was defined globally and integrated over finite horizons creating boundary
 235 behaviour that emerged naturally from the exact analytic integral. Therefore, the top horizon collapses
 236 to a point evaluation at $z = 0$, the basal horizon to $z = 1$ and interior horizons are governed by the
 237 integral means of the stiffness process. Smoothing was thus confined strictly to the soil domain,

238 preventing boundary drift, align with the constraint matrix, while maintaining physically consistent
239 continuity and curvature.

240 Data continuity between horizons represents a physical requirement for mass conservation and structural
241 integrity. These constraints were encoded in a Jacobian matrix G , enforcing both C^0 and C^1 continuity
242 across horizons:

243
$$\|G\beta\|_2^2 = G\beta = 0,$$

244
$$f_j(h_j) - f_{j+1}(0) = 0 \text{ } (C^0 \text{ continuity}),$$

245
$$f'_j(h_j) - f'_{j+1}(0) = 0 \text{ } (C^1 \text{ continuity}),$$

246

247 Boundary slope constraints were applied at the top and bottom of the profile to anchor the spline, maintain
248 numerical stability and maintain a mathematically steady state. Together with R , the boundary conditions
249 create a zero flux and geogenic boundary for the top and bottom horizon, respectively. To enforce all
250 constraints exactly while retaining a linear system, the coefficient vector was projected into the null-
251 space of G :

252
$$\beta = N\gamma,$$

253 where N spans the null-space of G . Within this projected space, the horizon-level roughness penalties
254 R_j are combined into a global, profile-aware roughness matrix, representing the total energetic cost of
255 profile deformation:

256
$$R = N^T \left(\sum_j R_j \right) N$$

257 This transformation converts the constrained energy minimisation problem into an unconstrained system
258 in γ , ensuring exact horizon continuity while preserving the physical interpretability of the roughness

259 penalty. In this way, continuity constraints were satisfied exactly, the roughness penalty remained
260 physically interpretable and the solution efficiently balances fidelity to observed data with minimisation
261 of the profile's potential energy. The objective function is then formulated as:

$$262 \quad \mathcal{L}(\gamma) = \frac{1}{2} \| y - AN\gamma \|_2^2 + \lambda_r \gamma^\top N^\top RN\gamma.$$

263 Solving for γ yields the reduced-order ordinary least squares solution, and the full coefficient vector is
264 recovered as $\beta = N\gamma$. This approach guarantees exact horizon continuity while balancing smoothness
265 against fidelity to the observed data. Crucially, the roughness term R arises from the definite integral of
266 the Euler cumulative mass process, embedding global, depth-dependent stiffness directly into the loss
267 function. The governing system is linear and reflects steady-state physics, and the phySpline solution is
268 obtained analytically through energy minimisation, producing an optimal, closed-form set of coefficients
269 that captures physically consistent curvature and emergent boundary behaviour across the profile.

270 Once a spline's coefficients were estimated, the integral for any standardised depth interval can be
271 directly calculated or continuous curves can be interpolated and fitted values $f_i(x)$ are mapped to soil
272 classes by nearest latent class (Table 1):

$$273 \quad c_i = \arg \min_i | f_i(x) - l_i |,$$

274 where l_i are latent class values and c_i is the interpolated soil texture class at location (e.g., interval, cm,
275 mm, etc) i . This approach provides a simple, computationally efficient and intuitive classification of the
276 full vertical soil profile.

277 2.2.4 Generalisation and missing horizons

278 Many studies have discussed the idea of adding pseudo horizons to anchor boundary conditions at the
279 top and bottom of the profile or as an anchor when there are discrete boundaries (Bishop et al., 1999;
280 Malone et al., 2009; Odgers et al., 2012; Ponce-Hernandez et al., 1986). Notably, many authors noted

281 challenges with abrupt changes or the “drift” effect common in quadratic splines. To handle missing or
282 unsampled depths, pseudo horizons were introduced to stabilise phySpline coefficients. Missing depths
283 were initially imputed using the median of adjacent horizons, providing placeholders for coefficient
284 estimation. Once spline coefficients were computed, imputed horizons were removed from the system
285 and treated as extrapolated regions. However, no pseudo-horizon was added to address drift, as the
286 energy-minimising solution naturally curves back to a vertical slope.

287 2.2.5 Spatial prediction

288 At the provincial scale, harmonised soil texture classes were predicted across the 90 m Soil and
289 Landscape Grids of Australia (ASRIS, 2024; CSIRO, 2024) to provide spatial representations and
290 visualise vertical variation along transects. Predictions were generated for six standard depth intervals,
291 using 18 covariates representing clay, silt, and sand fractions within each depth interval (Malone and
292 Searle, 2022; Viscarra Rossel et al., 2014). Gradient tree boosting was used for spatial prediction due to
293 its ability to capture complex environmental relationships without over-predicting dominant soil classes
294 (Flynn et al., 2019). Gradient tree boosting is an eager learner that precomputes a model during training
295 (from soil profiles), making prediction across grids computationally efficient (Hastie et al., 2009; Kuhn
296 and Johnson, 2013). For each depth interval, all grid layers were used as covariates, i.e., the independent
297 variables consisted of texture fractions from 0–200 cm. Mathematically, the predicted soil texture class
298 \hat{C}_k for class k is:

$$299 \quad \hat{C}_k \approx \sum_{m=1}^M L_m H_m(\text{clay}_k, \text{silt}_k, \text{sand}_k),$$

300 where M is the total number of trees, L_m is the learning rate, and H_m is the m -th tree in the sequence,
301 trained to iteratively improve predictions from the previous tree.

302 2.3 Validation and plausibility

303 2.3.1 Reference splines

304 Two reference splines (controls) were implemented to illustrate the methodological progression from
305 standard continuous interpolation to the phySpline framework. This progression is intended as a
306 demonstration of specific enhancements, rather than a formal comparative study, highlighting the steps
307 required to resolve categorical transitions while retaining the simplicity and statistical robustness of the
308 ea-spline framework.

309 The first reference spline, C-EAS was a canonical ea-spline adapted to classify where data fidelity was
310 the geometric mean, and the regularization term was the first derivative penalty. Therefore, continuity is
311 implicitly implied through the geometry of the fidelity term

$$312 \quad \mathcal{L}_{C-EAS}(\beta) = \frac{1}{2} ||A\beta - y||_2^2 + \lambda_r \beta R \beta.$$

313 The C-SoftG reference spline was a non-canonical intermediate spline where there is a trade off between
314 data fidelity, smoothness and continuity. The terms are the same as the ea-spline and continuity matrix
315 is the same as the phySplines,

316

$$317 \quad \mathcal{L}_{C-SoftG}(\beta) = \frac{1}{2} ||A\beta - y||_2^2 + \lambda_r \beta R \beta + ||G\beta||_2^2.$$

318 2.3.2 Statistical validation

319 PhySpline performance was evaluated across multiple scales using overall accuracy, Cohen's kappa
320 (Cohen, 1960) and the latent value Root Mean Squared Error (RMSE) for λ_r values of 0.5, 0.25, 0.10,
321 0.05 and 0.01. These values were selected following Bishop et al. (1999) and other studies on ea-splines
322 such as Malone et al. (2009) and . This approach ensured that scale-specific performance reflected
323 robustness to data availability, rather than simply spatial extent, providing a controlled stress test. To

324 select an appropriate λ_r for the control and subsequent analyses, a sensitivity analysis was performed
325 using L-curve curvature maximisation at the global scale. The “elbow” of the curve, corresponding to
326 the peak of the second derivative of the LOESS-smoothed RMSE profile, identifies the transition
327 between under- and over-fitting.

328 For individual soil texture classes, recall (producer’s accuracy), precision (user’s accuracy), bias and F1
329 scores were calculated to evaluate the ability of phySplines to classify both dominant and
330 underrepresented classes. Harmonised uncertainties were quantified as the absolute distance between
331 predicted values and the nearest latent class, providing a measure of confidence across both occupancy
332 and transitional classes. These uncertainties were subsequently scaled to a range of 0–1.

333 Spatial predictions were evaluated in a similar manner, using an 80/20 split for training and evaluation.
334 Overall accuracy was computed to assess predictive performance. While the primary focus of this study
335 is phySpline performance, evaluation of spatial predictions ensured that mapped representations of soil
336 texture are meaningful, reliable for visualisation purposes and were comparable to other studies.

337 2.3.3 Physical plausibility

338 To evaluate the behaviour and physical consistency of the phySpline solutions, we computed a set of
339 diagnostics for profile:

- 340 • Kink (C^1 Continuity): The absolute difference between the bottom slope of one horizon and the
341 top slope of the next, capturing derivative discontinuities at horizon boundaries.
- 342 • Energy (Roughness): The quadratic form $\beta^T R_s \beta$ for each horizon, representing the contribution
343 of the horizon to the spline’s regularisation term. Higher energy indicates significant internal
344 “stretching” to accommodate the data.

345 • Mass jump (Mass): The ratio of horizon thickness h_j to the total profile depth H_{tot} , representing
 346 the volumetric leverage of the layer.

347 • Mismatch (C^0 Continuity): The absolute difference between the predicted value at the base of
 348 horizon j and the intercept of horizon $j + 1$, quantifying value discontinuities across horizons.

349 These diagnostics provide complementary measures of smoothness, physical realism, and horizon-level
 350 behavior, allowing both global and horizon-specific assessment of spline performance.

351 To summarise spline physical plausibility, we combined the diagnostics into a composite metric. Let K_i
 352 denote the interfacial kink, E_i the internal energy, M_j the horizon mass jump, and $M_{m,i}$ the boundary
 353 mismatch. Weighted root-mean-square (RMS) values were computed for kink and energy as:

354
$$K_{\text{RMS}} = \sqrt{\frac{\sum_{i=1}^n (K_i M_j)^2}{\sum_{i=1}^n M_j}}$$

356
$$E_{\text{RMS}} = \sqrt{\frac{\sum_{i=1}^n (E_i M_j)^2}{\sum_{i=1}^n M_j}}.$$

355

357 The RMS of mismatch is calculated as:

359
$$\text{Mismatch}_{\text{RMS}} = \sqrt{\frac{1}{n} \sum_{i=1}^n M_{m,i}^2}.$$

358

360 Weighting kink and energy by M_j ensures that structural integrity of the primary soil mass is prioritized
361 over localized noise in thin horizons. The Integrated Process Score (ISP) metric is then defined as the
362 average of these three RMS values:

$$363 \quad ISP = \frac{Kink_{RMS} + Energy_{RMS} + Mismatch_{RMS}}{3}.$$

364 To assess whether predicted classes preserve information from observed classes, Mutual Information
365 (MI) was calculated:

$$366 \quad I(X; Y) = \sum_{x \in X} \sum_{y \in Y} p(x, y) \log \left(\frac{p(x, y)}{p(x)p(y)} \right),$$

367 where X is the observed soil texture class, Y the predicted class, $p(x, y)$ the joint probability of $X = x$
368 and $Y = y$, and $p(x), p(y)$ the marginal probabilities. MI was normalized to the range [0,1] by dividing
369 by the maximum MI within each group. This captures transitions across the two-dimensional structure
370 of Depth \times Classes [1–12], which would be missed in a one-dimensional, depth-only analysis (e.g.,
371 continuous depth).

372 This formulation favors economical, process-clamped solutions, where latent profiles transition smoothly
373 with depth. It serves as a structural validation metric, ensuring that spline-derived numeric values
374 produce a physically consistent soil column before categorical assignment. In other words, MI quantifies
375 how much information the predictions preserve about observed classes while maintaining realistic, depth-
376 continuous transitions.

377 3 Results

378 3.1 Comparisons

379 The results of the phySpline at each scale followed the same general pattern (Table 2). As λ_r decreased,
380 phySpline performance increased, with higher accuracy, kappa values and lower latent-space errors.

381 These patterns, however, were most pronounced at the global scale with an 80% reduction in λ_r (from
382 0.50 to 0.10) resulting in a 44% increase in kappa, from 0.76 to 0.95. A further 90% reduction in λ_r (from
383 0.10 to 0.01) was associated with a 4% increase in kappa, from 0.95 to 0.99. The corresponding RMSE
384 decreased from 0.37 at $\lambda_r = 0.50$ to 0.13 at $\lambda_r = 0.10$ (65% decrease in errors), and further to 0.02 at
385 $\lambda_r = 0.01$ (85% decrease in errors). Therefore, there is a strong relationship between λ_r , accuracy, kappa
386 and RMSE. Thus, the elbow method on the global data revealed a $\lambda_r = 0.10$ was the slope steepened
387 past this point indicating potential overfitting.

388 *Table 2: The scale, lambda (λ_r), overall accuracy, kappa and the latent RMSE.*

Scale	λ_r	Accuracy (%)	Kappa	RMSE
<i>Global</i>	0.50	70	0.66	0.37
	0.25	89	0.89	0.21
	0.10	97	0.96	0.11
	0.05	100	1.00	0.01
	0.01	100	0.99	0.02
<i>Provincial</i>	0.50	77	0.72	0.37
	0.25	87	0.83	0.25
	0.10	96	0.94	0.13
	0.05	100	0.99	0.02
	0.01	100	1.00	0.02
<i>Local</i>	0.50	78	0.72	0.34
	0.25	92	0.89	0.23
	0.10	97	0.96	0.12
	0.05	100	1.00	0.01
	0.01	100	1.00	0.02

389

390 At the provincial scale, kappa increased from 0.66 at $\lambda_r = 0.50$ to 0.94 at $\lambda_r = 0.10$, reaching 1.00 at
391 $\lambda_r = 0.05$. Over the same range, RMSE decreased from 0.37 to 0.13 and then to 0.02. over the same
392 range. At the local scale, kappa increased from 0.72 at $\lambda_r = 0.50$ to 0.96 at $\lambda_r = 0.10$, and to 1.00 at
393 $\lambda_r = 0.05$. The RMSE decreased from 0.34 to 0.12 and to 0.02 across the same range.

394 The C-SoftG control achieved statistical performance comparable to phySpline across all scales (Table
395 3). At the global scale, accuracy reached 97%, with a kappa of 0.96 and an RMSE of 0.14. At the
396 provincial scale, accuracy, kappa, and RMSE were 95%, 0.90, and 0.14, respectively. At the local scale,
397 C-SoftG achieved an accuracy of 93%, a kappa of 0.90, and an RMSE of 0.19. The C-EAS had nearly
398 perfect statistical performance at all scales.

399 *Table 3: The reference splinel accuracy-based measures showing the scale, λ_r , overall accuracy, kappa, RMSE of the residuals
400 and the uncertainties of the harmonised depth intervals.*

Spline	Scale	λ_r	Accuracy	Kappa	RMSE
<i>C-SoftG</i>	Global	0.10	97	0.96	0.14
	Provincial	0.10	95	0.93	0.14
	Local	0.10	93	0.90	0.19
<i>C-EAS</i>	Global	0.10	100	1.00	<0.01
	Provincial	0.10	100	1.00	<0.01
	Local	0.10	100	1.00	<0.01

401

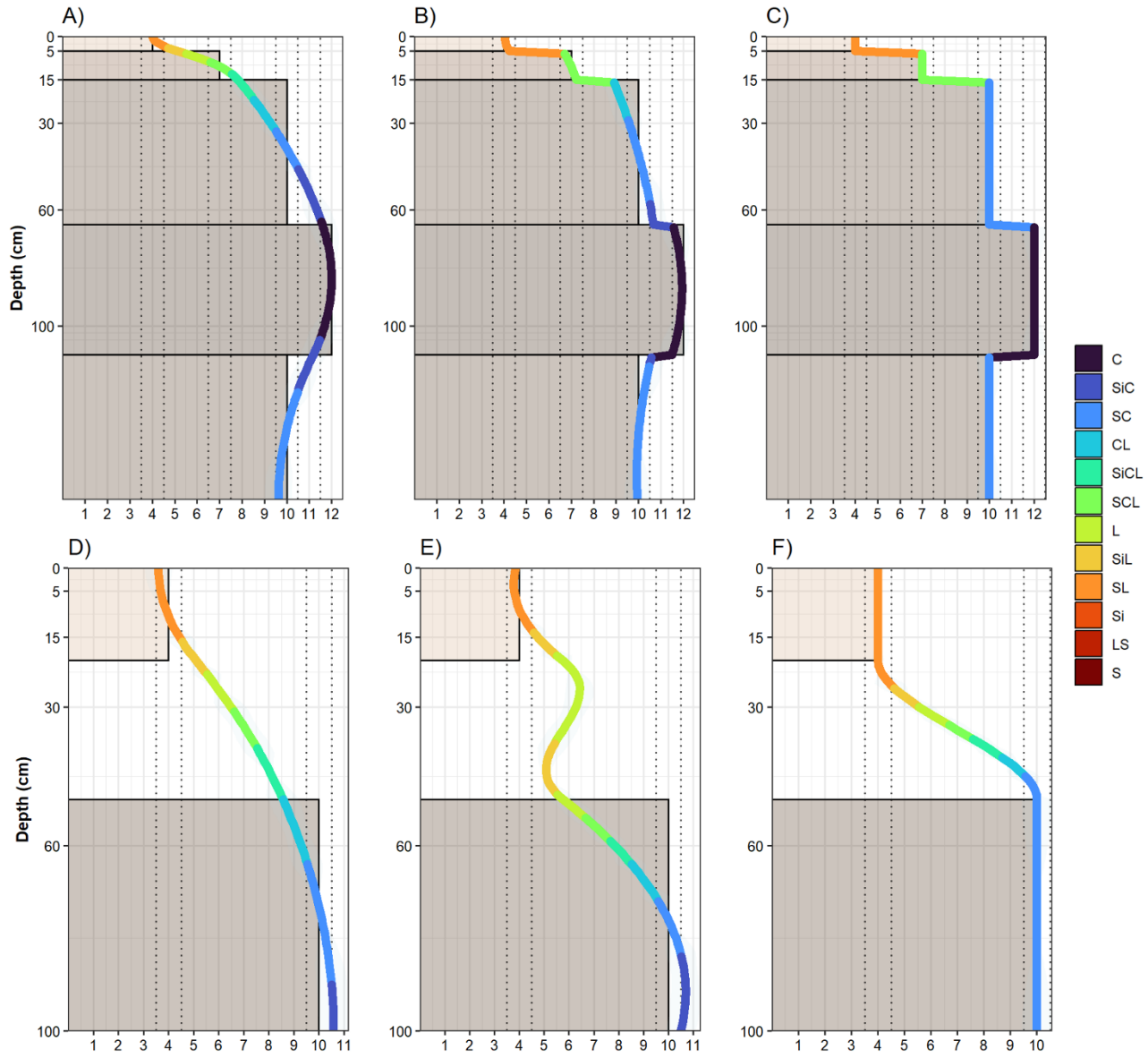
402 At all scales, the IPS is comparatively lower with 0.15, 0.31 and 0.15 for the global, provincial and local
403 scales respectively. However, all indices were best performing at the global scale with the lowest IPS
404 and highest MI (1.00). The provincial scale, similar to the statistical analysis, had moderate performance
405 with a slightly higher MI of 0.85 and the local scale had a MI of 0.88. It should be noted that these results
406 are not comparable across models as the curves are fitted in different ways and the energy indicates a

407 different measure. However, the C-SoftG had the same trend and C-EAS technically doesn't have these
408 measures but were gathered anyways to see if they were like the statistics and produce misleading results.

409 *Table 4: Process based parameters showing mean energy, kink, MassJump, mismatch, Integrated Process Score (IPS) and*
410 *Mutual Information (MI).*

Spline	Scale	Kink	Energy	MassJump	Mismatch	IPS	MI
phySpline	Global	0.00	0.14	0.20	0.00	0.15	1.00
	Provincial	0.00	0.58	0.29	0.00	0.31	0.85
	Local	0.00	0.49	0.30	0.00	0.15	0.88
C-SoftG	Global	0.01	0.26	0.20	0.41	0.43	0.94
	Provincial	0.00	0.60	0.29	4.00	3.14	0.85
	Local	0.00	0.61	0.30	1.85	1.69	0.85
C-EAS	Global	0.00	0.00	0.20	17.7	9.60	1.00
	Provincial	0.00	0.00	0.29	23.0	11.5	1.00
	Local	0.00	0.00	0.30	16.6	7.60	1.00

411 .
412 Figure 3A–C presents example soil profiles illustrating continuity, mismatch, kink behavior and class–
413 process alignment for the three models. The phySpline (Figure 3A) produced a smooth latent profile that
414 crossed horizon boundaries exactly at observed class transitions while also resolving intermediate
415 transitional classes along the latent scale. In contrast, the C-SoftG model correctly interpolated each
416 horizon to its observed class but showed erratic curvature and limited representation of transitional
417 classes between horizons (Figure 3B). The C-EAS model achieved perfect classification accuracy;
418 however, the fitted curve and resulting classes strictly followed horizon boundaries allowing no transitory
419 behaviour, yielding no meaningful internal structure beyond exact mathematical conformity (Figure 3C).



420

421 *Figure 3: Selected profiles to demonstrate curves from the phySpline (A), the control C-SoftG (B), the control (C), missing*
 422 *horizons with phySplines (D), C-SoftG without ghost horizons (E) and C-EAS without ghost horizons (F).*

423 Figure 3E–G show extrapolated profiles for the phySpline, C-SoftG (without a ghost horizon) and C-
 424 EAS (without a ghost horizon). The phySpline maintained smooth, physically coherent transitions under
 425 extrapolation (Figure 3E), whereas the absence of a ghost horizon in C-SoftG resulted in increased
 426 instability near profile boundaries (Figure 3F). The C-SoftG model was evaluated without a ghost horizon
 427 to illustrate the effects of extrapolation in the absence of artificial anchoring, whereas ghost horizons

428 were used for all other C-SoftG analyses. Notably, C-EAS captured transitional classes more effectively
429 when horizons were absent, but this behavior was suppressed when horizons were present (Figure 3G).

430 3.2 Global scale

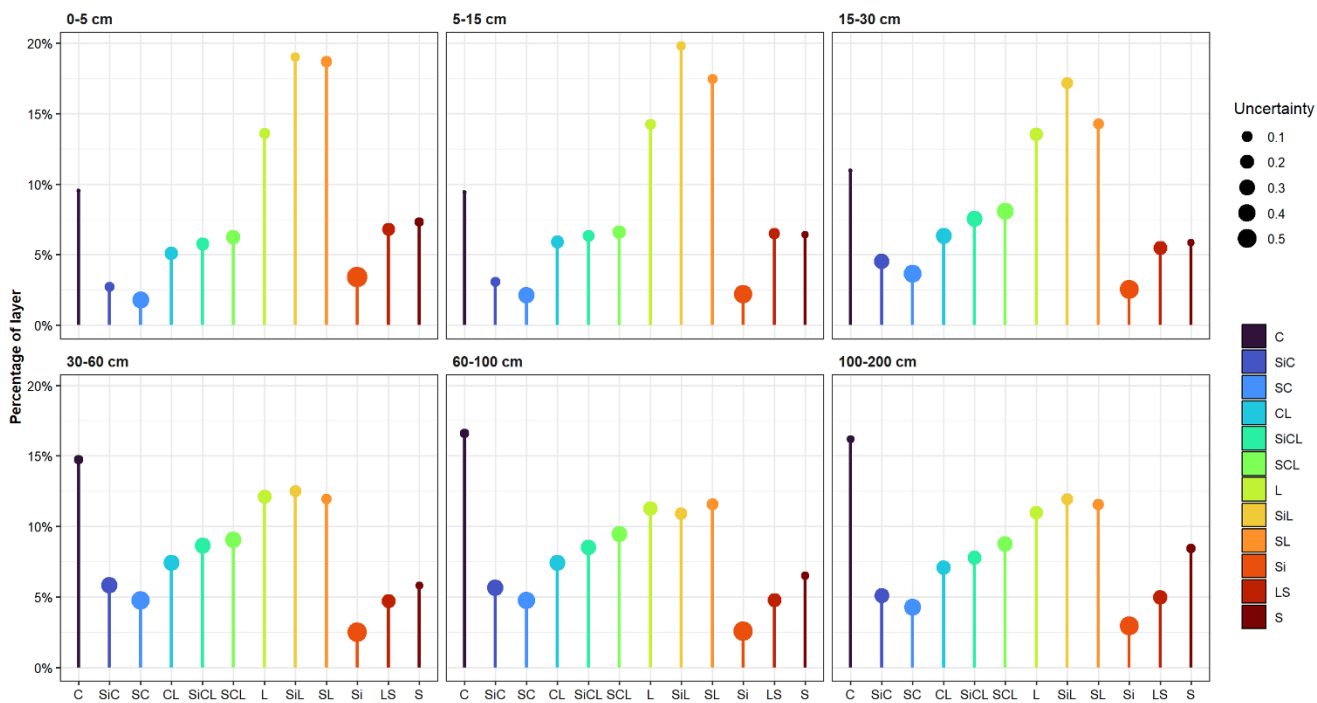
431 The global model took 8 min and 40.09 seconds to run 101,568 profiles through the linear ODE equation.
432 Despite moderate class imbalance (observed occurrence ranging from 16.2% for SL to 0.41% for Si), all
433 classes achieved F1 scores ≥ 0.80 except Si (F1 = 0.58; Table 4). Absolute occupancy bias remained
434 within ± 1.00 percentage points for all classes except C (-1.20), with the C class (14.0% observed
435 occupancy) slightly underpredicted. The Si class exhibited high recall (0.90) but low precision (0.43),
436 reflecting increased false-positive assignment for this rare texture class, which was slightly over
437 predicted. All other soil texture classes had unbiased predictions according to a 1.00% threshold.

438 *Table 5: The observed prevalence and predicted prevalence, prediction bias, precision, recall and F1 scores at the global scale.*

Class	Observed (%)	Predicted (%)	Bias	Precision	Recall	F1
C	14.0	12.8	-1.20	1.00	0.91	0.95
SiC	4.70	5.28	0.58	0.78	0.87	0.82
SC	2.17	2.70	0.54	0.74	0.92	0.82
CL	7.50	7.25	-0.25	0.95	0.92	0.93
SiCL	8.36	8.56	0.19	0.92	0.94	0.93
SCL	7.47	7.71	0.24	0.91	0.93	0.92
L	12.6	13.1	0.58	0.91	0.95	0.93
SiL	14.7	14.6	-0.11	0.95	0.93	0.94
SL	16.2	15.5	-0.64	0.99	0.95	0.97
Si	0.41	0.86	0.45	0.43	0.90	0.58
LS	5.94	5.91	-0.04	0.95	0.94	0.94
S	5.91	5.59	-0.33	0.99	0.94	0.97

439
440 Class occupancy of harmonised depth intervals revealed systematic vertical trends in global soil texture
441 distributions (Figure 4). Clay content increased with depth, rising from 9.40% at 5–15 cm to 16.60% at
442 60–100 cm (76% increase). However, stronger depth-related increases were observed for SiC and SC.
443 The SiC class increased from 2.73% at 0–5 cm to 5.81% at 30–60 cm (113% increase), followed by a

444 slight decline to 5.09% at 100–200 cm. SC increased from 1.79% at 0–5 cm to 4.75% at 60–100 cm
 445 (166% increase). Both SiC and SC exhibited higher associated uncertainty, with mean uncertainty values
 446 of 0.27 and 0.39, respectively. Silty loam decreased from 19.8% at 5–15 cm to 10.9% at 60–100 cm (45%
 447 change), while SL declined from 18.7% at 0–5 cm to 11.5% at 100–200 cm (38% change). These classes
 448 exhibited comparatively low median uncertainty (0.15 for SiL and 0.14 for SL). In contrast, S showed
 449 minimal depth dependence, with only a 31% change across the profile, decreasing to 23% occupancy at
 450 depth.



451

452 *Figure 4: The percent proportion of each soil texture class for the GlobalSoilMap depth intervals with their uncertainties.*

453 Depth-resolved structural diagnostics of the phySpline profiles revealed systematic variation across
 454 the harmonised depth intervals (Table 6). The phySpline was computationally zero for kink and mismatch
 455 was expected. For energy, it ranged from 0.314 at 100-200 cm to 0.493 at the 0-5 cm range when
 456 corrected for depth width. This mirrors the IPS which also slowly declined with depth from 0.164 to
 457 0.104, while MI was over 0.99 and remained independent of depth.

Table 6: Process-based validation showing the root mean square of Kink_{rms} , $\text{Energy}_{\text{rms}}$, IPS and MI

Spline	Intervals	Kink_{rms}	$\text{Energy}_{\text{rms}}$	$\text{Mismatch}_{\text{rms}}$	IPS	MI
<i>PhySpline</i>	0-5 cm	0.000	0.493	0.000	0.164	0.998
	5-15 cm	0.000	0.409	0.000	0.136	0.999
	15-30 cm	0.000	0.391	0.000	0.130	0.998
	30-60 cm	0.000	0.378	0.000	0.126	0.999
	60-100 cm	0.000	0.359	0.000	0.120	0.998
	100-200 cm	0.000	0.314	0.000	0.104	0.996
<i>C-SoftG</i>	0-5 cm	0.004	0.191	1.478	0.557	0.992
	5-15 cm	0.004	0.153	1.227	0.461	0.975
	15-30 cm	0.004	0.150	1.293	0.482	0.942
	30-60 cm	0.004	0.140	1.245	0.463	0.921
	60-100 cm	0.005	0.128	1.212	0.450	0.922
	100-200 cm	0.003	0.107	1.395	0.501	0.941
<i>C-EAS</i>	0-5 cm	0.000	0.000	31.79	10.69	1.00
	5-15 cm	0.000	0.000	29.49	9.829	1.00
	15-30 cm	0.000	0.000	31.58	10.53	1.00
	30-60 cm	0.000	0.000	31.22	10.40	1.00
	60-100 cm	0.000	0.000	32.33	10.78	1.00
	100-200 cm	0.000	0.000	33.62	11.21	1.00

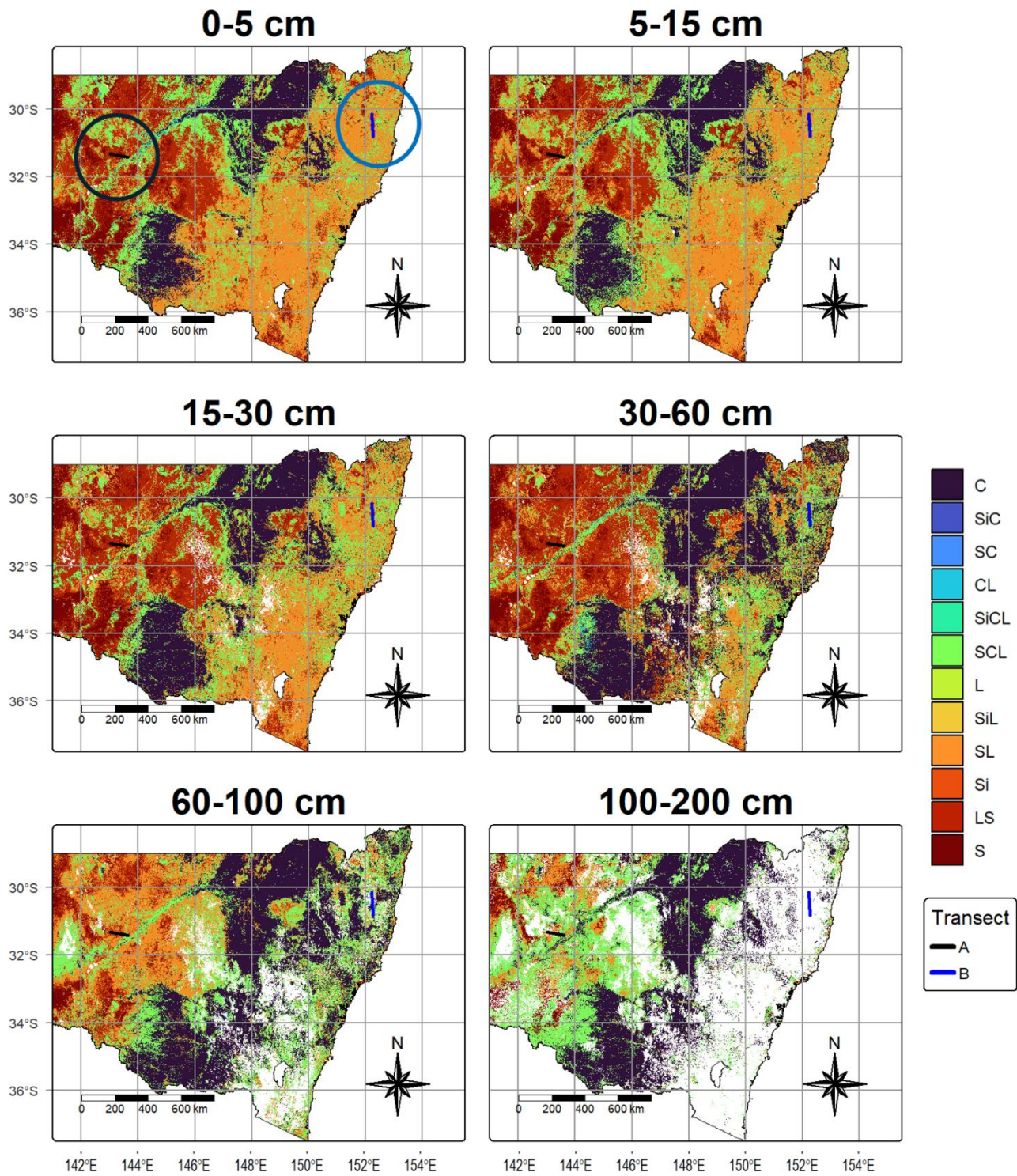
The composite IPS, integrating kink, energy and mismatch, decreased with depth from 0.165 in the 0–5 cm interval to 0.105 in the 100–200 cm layer, highlighting progressively lower structural penalties in deeper horizons. These patterns were consistent across more than 1.5 million horizon-level observations,

463 with the number of profiles per interval ranging from 140,031 (0–5 cm) to 610,964 (30–60 cm). The C-
464 SoftG Kink ranged from 0.00334 at 100–200 cm to 0.00415 at 0–5 cm. The Energy decreased from 0.191
465 at 0–5 cm to 0.107 at 100–200 cm, whereas Mismatch remained elevated (1.22–1.47), reflecting less
466 precise horizon alignment than phySpline. The depth-resolved IPS ranged from 0.451 at 60–100 cm to
467 0.557 at 0–5 cm. Profile counts matched those of phySpline, enabling direct comparison.

468 The C-EAS profiles showed minimal interfacial discontinuities (Kink $1.13\text{--}2.79 \times 10^{-16}$) and negligible
469 internal roughness (Energy $\sim 10^{-29}$), but exhibited very large boundary misalignments (Mismatch 29.5–
470 33.6), resulting in correspondingly high IPS values (9.83–11.2). Depth trends were relatively stable
471 across intervals, with shallow layers (0–5 cm) showing slightly lower IPS than deeper horizons. The MI
472 scores with harmonised depths follow that of the whole profile with all C-EAS having the highest MI
473 followed by phySplines and C-SoftG.

474 3.2 Provincial scale

475 This visualisation approach required spatial analysis from the phySplines prior to implementation at
476 the provincial scale. The spatial classification accuracy was approximately 50% across depth intervals,
477 with a maximum of 54%. Similar spatial accuracies, despite good depth-function performance and
478 realistic class distributions, have been reported previously (Flynn et al., 2024, 2022a). In this case, the
479 spatial results were sufficient to support further profile-level analysis. Two transects, indicated by black
480 and blue circles in the 0–5 cm layer and the black and blue transects (length $\approx 60\text{--}70$ km) of the predicted
481 classes (Figure 5), were therefore selected for visualisation of phySpline behaviour.



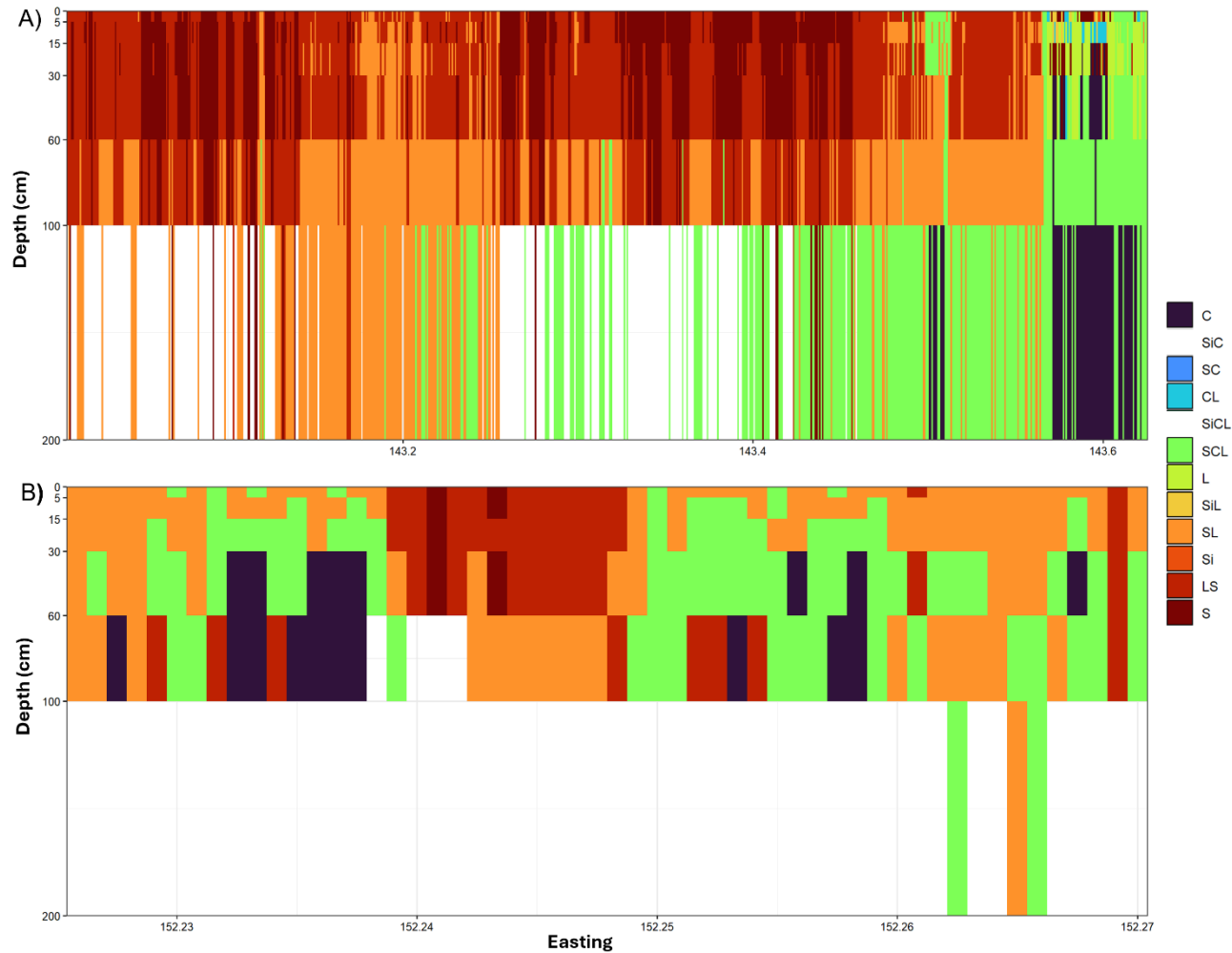
482

483 *Figure 5: Predictions for New South Wales, Australia using phySpline harmonised texture classes as training data.*

484 Both transects span approximately 60–70 km. Transect A is located in the semi-arid western region and

485 runs west to east, while transect B traverses the more topographically variable, subtropical eastern region

486 from north to south. Transect A captures a higher number of pixels, providing finer spatial detail, whereas
 487 transect B covers a larger pixel area, resulting in a coarser but simplified visualisation. These transects
 488 illustrate differences in spatial resolution and visual representation across contrasting landscapes.



489

490 *Figure 6: Cross sections used to display transects of the soil texture class (A) and each transect with depth intervals (B,C). The*
 491 *transects x-axis runs latitude or from west to east.*

492 The provincial scale exhibited the greatest class imbalance (Table 7), with C occupying 40% of the
 493 dataset, yet it was underpredicted by less than 1.00% and remained with balanced predictions. In contrast,
 494 the spline overpredicted the SiC class, but only by 0.67% and misclassification decreased gradually away

495 from the dominant class in a systematic manner. Therefore, although the dataset was imbalanced, the
 496 predictions remained balanced and like the global scale.

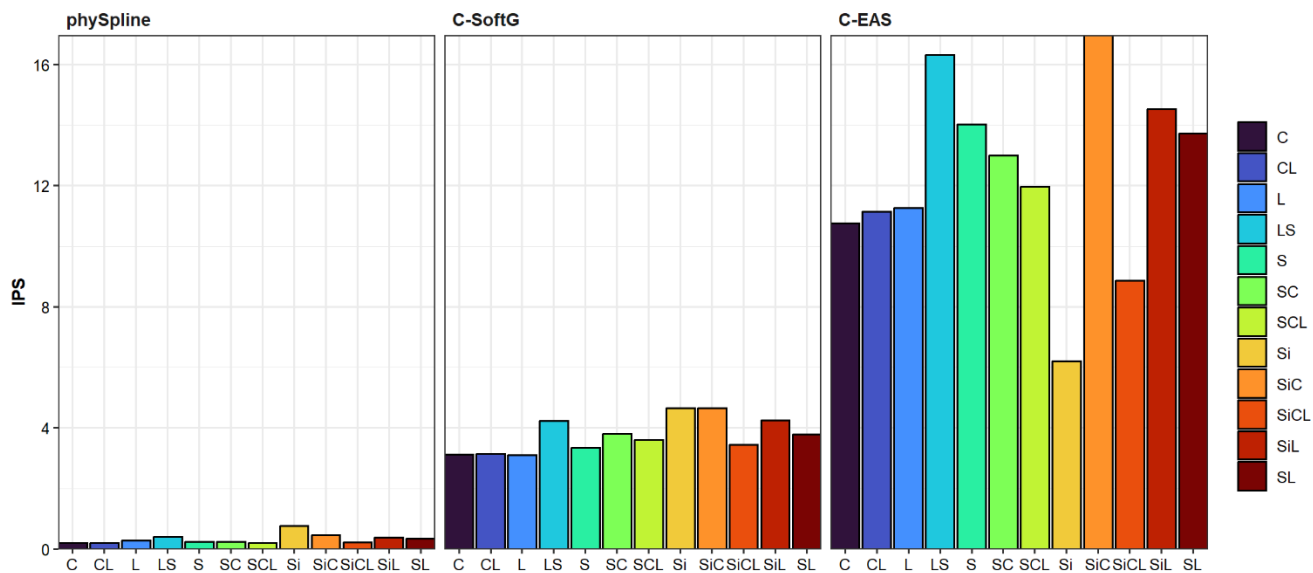
497 *Table 7: Confusion matrix for from phySplines interpolation on the WoSIS dataset in NSW, Australia.*

	C	SiC	SC	CL	SiCL	SCL	L	SiL	SL	Si	LS	S	Recall
<i>C</i>	8665	343	32	3	1	0	0	0	0	0	0	0	0.96
<i>SiC</i>	0	52	4	1	0	0	0	0	0	0	0	0	0.91
<i>SC</i>	0	7	1122	52	2	1	0	0	0	0	0	0	0.95
<i>CL</i>	0	0	16	1060	24	2	0	0	0	0	0	0	0.96
<i>SiCL</i>	0	0	0	0	44	3	0	0	0	0	0	0	0.94
<i>SCL</i>	0	0	1	14	161	3786	56	6	0	0	0	0	0.94
<i>L</i>	0	0	0	0	1	19	919	3	1	0	0	0	0.97
<i>SiL</i>	0	0	0	0	0	1	7	75	0	0	0	0	0.90
<i>SL</i>	0	0	0	0	0	4	5	145	3707	8	0	0	0.96
<i>Si</i>	0	0	0	0	0	0	0	0	0	3	0	0	1.00
<i>LS</i>	0	0	0	0	0	0	0	2	7	78	1313	0	0.94
<i>S</i>	0	0	0	0	0	0	0	0	2	5	24	793	0.96
<i>Precision</i>	1.00	0.13	0.95	0.94	0.19	0.99	0.93	0.32	0.99	0.03	0.98	1.00	0.96

498
 499 The Si class, despite its low prevalence, exhibited an apparent 100% accuracy, while most other classes
 500 achieved accuracies above 90%, except for SiC (86% accuracy). The high false positives can be seen in
 501 all the low prevalence classes of SiC (13%), SiCL (19%), SiL (32%) and Si (3%) which had an original
 502 prevalence of 0.25, 0.20, 0.37 and 0.01 in the dataset, respectively. Therefore, although the high accuracy
 503 of each class, the precision and recall give insight into the transition classes.

504 Class-resolved structural diagnostics revealed systematic, method-specific differences in spline
 505 performance (Figure 7). For phySpline, IPS values remained low across all classes (0.20–0.77), with

506 contributions dominated by internal energy rather than boundary discontinuities or boundary
 507 mismatches. The lowest IPS was observed for coarse loams (CL = 0.20), whereas the highest occurred
 508 in fine silty textures (Si = 0.77), reflecting slightly higher internal variation in these classes. C-SoftG
 509 exhibited moderate energy penalties coupled with substantial boundary mismatches (IPS \approx 3–4.7),
 510 particularly in transitional textures such as SiL and SiC. In contrast, C-EAS displayed negligible Kink
 511 and energy penalties, but extreme boundary misalignments (IPS \approx 6–17) across all classes, highlighting
 512 its perfect local fit at the expense of global structural fidelity.



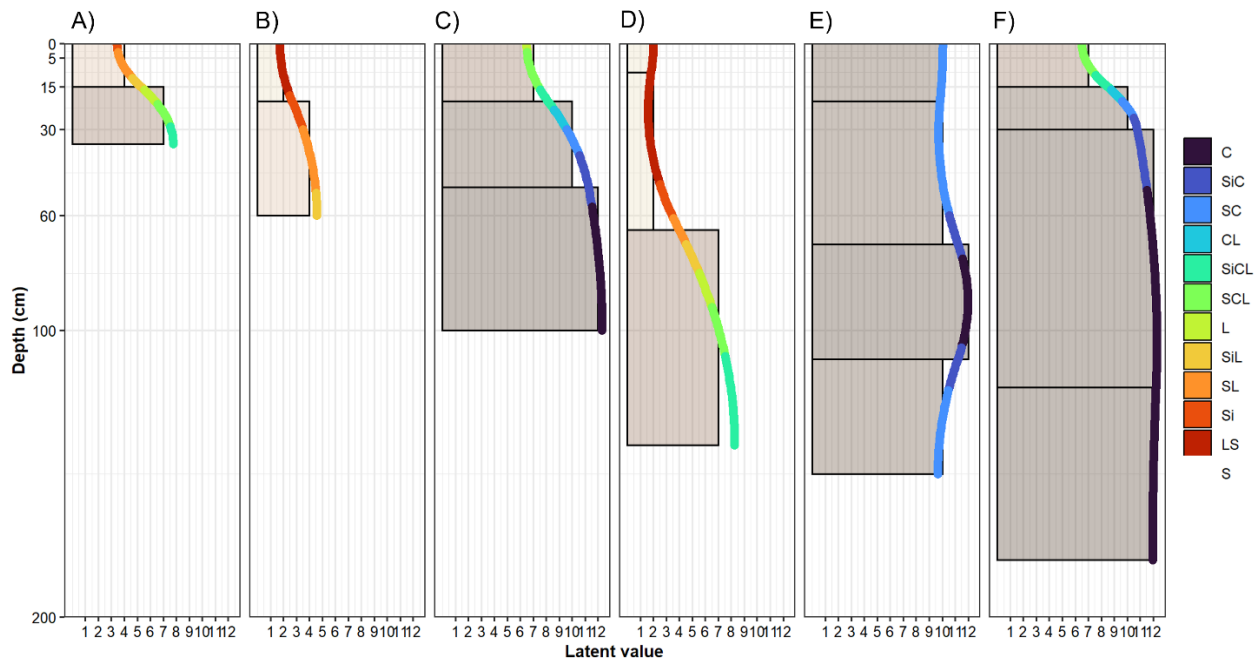
513

514 *Figure 7: The Integral Process Score (IPS) for the C-EAS, C-SoftG and the phySpline for and its correspondence to each class.*

515 3.3 Local scale

516 The Neno District dataset included 65 soil profiles with evenly represented soil texture classes (Figure
 517 8). The only comparison with the reference splines was if the splines were over constrained with 0.00,
 518 0.00 and 68.9 for the phySpline, C-SoftG and C-EAS, respectively. From these, six profiles were selected
 519 (Figure 2) for detailed analysis and overlaid with gridded environmental variables, including mean
 520 annual precipitation (MAP), mean annual temperature (MAT), elevation, slope, aspect and landform
 521 element (LFE). The selected profiles varied in depth, from shallow (Profile A, 35 cm) to deep (Profile F,

522 180 cm), and exhibited diverse texture patterns, ranging from shallow, coarse-textured profiles (Profile
 523 B, LS-SL, 35 cm) to deep, very fine textured soil (Profile E, SC-C, 150 cm). All profiles had low IPS of
 524 0.10, 0.06, 0.05, 0.20, 0.03 and 0.04 for A, B, C, D, E, F and G, respectively.



525
 526 *Figure 8: The selected profile's phySplines curve with their latent value on the y-axis to show how they correspond down the*
 527 *profile.*

528 The selected profiles represented a broad spectrum of pedogenetic factors, requiring a model capable of
 529 adapting to diverse depth and texture patterns (Table 8). Environmental conditions across the site ranged
 530 from high-altitude, high-precipitation mountain slopes to low-relief, high-temperature depositional
 531 hollows. Profile F was located at 1,419 m elevation with high annual rainfall (96 mm) on a steep slope
 532 (15.1%), whereas Profile D was in a low-relief hollow (2.16% slope) with lower rainfall (76 mm) and
 533 higher mean annual temperatures (24 °C). Profiles A, B and C represent intermediate conditions on slopes
 534 and spurs, with slopes ranging from 4.47 to 9.60 degrees reflecting the steep topography of the Neno
 535 region.

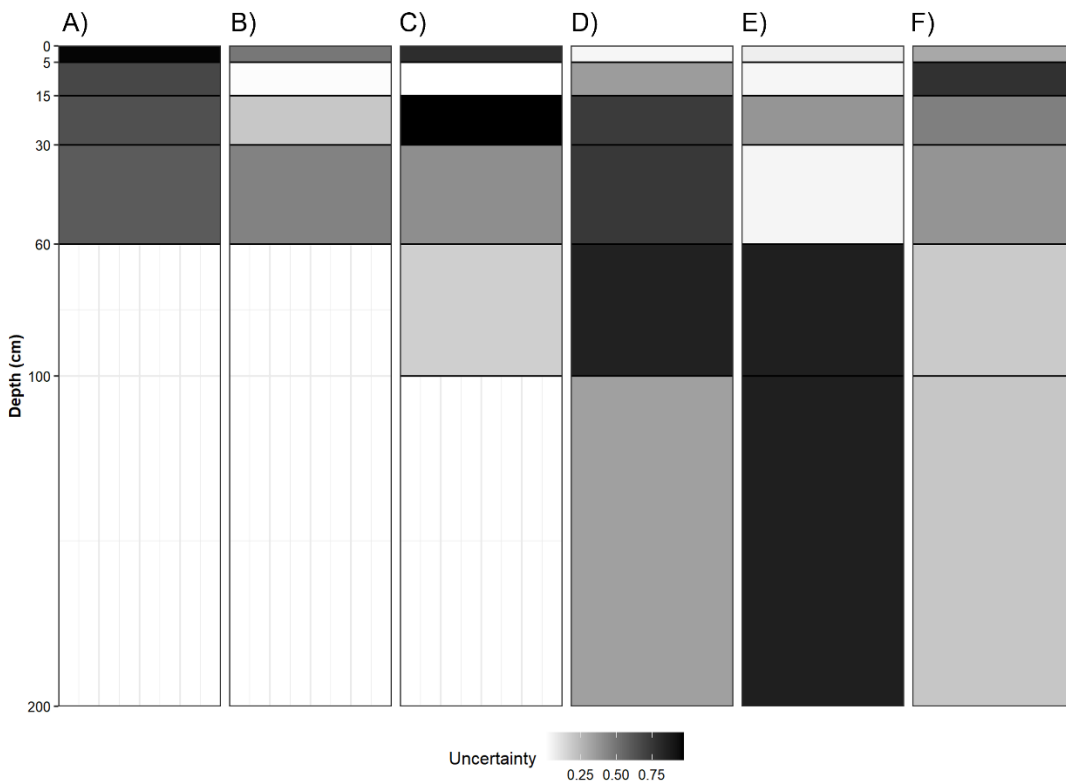
536 *Table 8: Environmental factors for each selected profile showing mean annual precipitation (MAP), mean annual temperature*
 537 *(MAT), elevation DEM, slope, aspect, landform element (LFE) and normalised mutual information per interpolated profile.*

Profile	MAP (mm)	MAT (°C)	DEM (m)	Slope (%)	Aspect	LFE	MI
A	80	24	521.0	4.47	203	Slope	0.63
B	73	25	358.0	4.49	93.5	Spur	0.63
C	97	22	951.0	9.60	297	Slope	1.00
D	76	24	442.0	2.16	145	Hallow	0.58
E	95	20	1,261	16.7	50.5	Spur	0.51
F	96	19	1,419	15.1	119	Spur	0.95

538

539 The harmonised uncertainty profiles (Figure 9) provide a standardised measure of model confidence
 540 across soil horizons. These profiles capture uncertainty associated with the discrete depth intervals used
 541 in the phySpline solution, reflecting stability across harmonised depth intervals (Table 8). Uncertainty
 542 values appear to be largely independent of the phySpline curves and environmental factors. Thin layers
 543 exhibited both high and low uncertainty (e.g., A = 0.95, D = 0.03), while subsoil horizons (60–100 cm)
 544 also showed variable uncertainty (D = 0.75, E = 0.17). Profiles in contrasting landscape settings, such as

545 B in the Lisungwe valley with low rainfall and E in mountainous, steep terrain, displayed similar
546 uncertainty patterns at 5–15 cm (B = 0.01, E = 0.04).



547

548 *Figure 9: The uncertainties associated with the selected profiles shown for the harmonised soil depths.*

549 Major classes with substantial observations, such as C, SC, SCL, SL, LS and S, were accurately
550 predicted, showing recall values between 0.90 and 1.00. Some minor or sparsely represented classes
551 (e.g., SiC, CL, SiCL, SiL, Si) had no observations in the test set, resulting in undefined recall and
552 precision. Nevertheless, there were seven classes present in the dataset and 11 in the interpolated set. Yet
553 misclassifications were minimal and mostly occurred between closely related classes, such as SC and
554 SL, or SCL and L.

555

556

557 *Table 9: Confusion matrix of the phySplines interpolation on the WoSIS dataset in the Neno District, Malawi.*

	C	SiC	SC	CL	SiCL	SCL	L	SiL	SL	Si	LS	S	Recall
C	12	0	0	0	0	0	0	0	0	0	0	0	1.00
SiC	0	0	0	0	0	0	0	0	0	0	0	0	NA
SC	0	0	28	2	0	0	0	0	0	0	0	0	0.93
CL	0	0	0	0	0	0	0	0	0	0	0	0	NA
SiCL	0	0	0	0	0	0	0	0	0	0	0	0	NA
SCL	0	0	0	0	1	54	1	0	0	0	0	0	0.96
L	0	0	0	0	0	0	1	0	0	0	0	0	1.00
SiL	0	0	0	0	0	0	0	0	0	0	0	0	NA
SL	0	0	0	0	0	0	0	2	58	1	0	0	0.97
Si	0	0	0	0	0	0	0	0	0	0	0	0	NA
LS	0	0	0	0	0	0	0	0	0	1	49	0	0.98
S	0	0	0	0	0	0	0	0	0	0	0	3	100
Precision	1.00	0.00	1.00	0.00	NA	1.00	0.50	0.00	1.00	0.00	1.00	1.00	0.97

558

559

4 Discussion

560 Building on the foundation of previous work, we developed the phySpline: a categorical, physics-
 561 informed, and analytically solvable spline for interpolating soil classes with depth. The model is designed
 562 to capture pedological philosophy through gradient thresholds, where information is held in the form of
 563 potential energy within the soil profile, and resistance to change is governed by an Euler cumulative mass
 564 process. To illustrate its performance and novelty, we compared it against two reference spline: a
 565 modified equal-area spline capable of classification (C-EAS) and an intermediate spline incorporating a
 566 continuity matrix (C-SoftG). The splines were evaluated using the WoSIS dataset at global, provincial
 567 (NSW, Australia), and local (Neno District, Malawi) scales. Validation considered both statistical
 568 performance and physical realism to determine whether the observed spline behaviour reflected genuine
 569 pedological patterns or merely mathematical coincidences. This multi-scale evaluation highlights the
 570 ability of the phySpline to maintain process-based continuity, structural fidelity, and pedological
 571 interpretability across diverse soil environments.

572 4.2.1 Spline performance and lambda

573 Across all spatial supports, phySplines exhibited a consistent and interpretable relationship between the
574 regularisation parameter λ_r , predictive accuracy, kappa and RMSE (Table 2). Decreasing λ_r
575 systematically increased overall accuracy and agreement while reducing RMSE, demonstrating that λ_r
576 functions as a physically meaningful process-based control rather than a purely statistical tuning
577 parameter. At the global scale, an 80% reduction in λ_r (0.50 - 0.10) produced a disproportionate
578 improvement in model performance (kappa \approx 0.66 - 0.93; RMSE \approx 0.37 - 0.13), whereas further
579 reductions yielded diminishing returns. This clear inflection supported the use of the elbow criterion to
580 identify $\lambda_r = 0.10$ as the optimal point that balanced fidelity and generalisation.

581 The phySplines framework demonstrated exceptional numerical stability, maintaining structural integrity
582 even when λ_r was reduced to 1.0×10^{-5} . Unlike traditional splines, which typically exhibit erratic
583 "hooking" or oscillatory behaviour at low smoothing levels, phySplines remained physically consistent.
584 This stability is attributed to the Euler cumulative mass process, where depth-dependent resistance (e^{kz})
585 acts as an internal physical damper.

586 By prioritising the exact analytic integral of the mass reservoirs over pointwise midpoint estimates, the
587 model achieved kappa values of 0.94–0.96 without over-constraining the solution. The high fidelity to
588 horizon observations does not result in a "staircase" effect; instead, the minimisation of the weighted
589 Dirichlet Energy ensures that transitions between texture classes are represented as continuous gradients.
590 This allows for the capture of transitional states (the latent taxonomic shifts between horizons) that are
591 often lost in discrete classification or over-smoothed continuous models.

592 4.2.2 Physics-informed, process-based and self-regularised

593 The intent of the reference functions was not for benchmarking but to contextualise the progression from
594 purely statistical splines to a physics-informed, process-based formulation. While accuracy metrics alone

595 suggest broadly comparable performance at $\lambda_r < 0.10$, this can mask fundamental differences in
596 structural behaviour (Table 3). PhySplines uniquely enforced continuity through a null-space projection
597 and the integrals used, yielding exact slopes (zero kink, C^1), exact values (zero mismatch, C^0), horizon
598 boundaries space ($z \in [0, 1]$), and smooth internal curvature simultaneously. This contributed to low
599 internal potential energy and high mutual information, producing a physically realistic spline with strong
600 and independent class resolve. Even when horizons appeared visually discrete, maintaining mass
601 continuity when interpolating or harmonising to new depth intervals was critical, as it preserved the
602 integrity of pedogenic transitions and ensured that derived thresholds reflected the underlying, physically
603 coherent soil structure in unsampled locations (Table 4). The phySpline remained unconstrained for all
604 scales.

605 By contrast, the C-EAS achieved perfect local fits by construction but oversimplified profile structure
606 and suppressed transitional behaviour, resulting in extreme boundary mismatches at the profile scale
607 (high IPS and MI). This produced splines that were statistically enhanced but physically implausible,
608 effectively overfitting the data at the expense of continuity and was over-constrained for all scales.
609 Nevertheless, it reflects the philosophical view that soil classes are inherently discrete and may carry
610 limited physical meaning, a perspective of conceptual significance. The C-SoftG remained
611 unconstrained, with a moderate IPS and MI, allowed smoother transitions but sacrificed derivative
612 continuity and boundary alignment. PhySplines were the only approach to resolve these trade-offs
613 explicitly, embedding soil-process realism directly into the analytical solution rather than relying on post
614 hoc constraints.

615 Although MI was relatively high across all splines, Figure 3A demonstrates that phySplines maintained
616 continuity in both depth and latent space without disconnects between transitions. Visually, this indicates
617 that when harmonising soil texture classes, phySplines correctly integrate over the new depth interval.
618 Figure 3B and 3C illustrate latent value mismatches for C-SoftG and C-EAS, highlighting structural

619 divergence despite high numerical accuracy. Figure 3E shows the clear stability effect phySplines
620 pseudo-horizon had on the coefficients, while Figure 3F demonstrated the clear need to impute the
621 median. Unexpectedly, C-EAS transitions between classes without knowledge of a horizon, a behaviour
622 the deserves further investigation

623 These findings indicate that phySplines reconstruct vertically coherent soil profiles consistent with
624 pedogenic theory, reframing depth functions as minimising the potential energy of the soil profile through
625 the exact integral of the cumulative mass. By uniting visual fidelity, physical plausibility and categorical
626 integrity, phySplines provide a fully interpretable framework to see between horizons, capturing both
627 subtle and abrupt pedogenetic transitions in a continuous, process-informed manner.

628 4.2.3 Global scale: process realism and depth-structured soil behaviour

629 Having established that phySplines respond to regularisation in a scale-independent and physically
630 interpretable manner, the global-scale results demonstrated how this behaviour translated into
631 pedologically realistic depth structure. At this extent, phySplines maintained stable class behaviour
632 despite moderate imbalance in class frequencies (Table 5). Dominant texture classes were not amplified,
633 while rare classes were retained as meaningful components of the latent process space rather than
634 suppressed or absorbed. Misclassifications occurred primarily among neighbouring texture classes,
635 reflecting transitional uncertainty rather than categorical failure. This behaviour is consistent with
636 pedological expectations, where soil texture transitions were gradual and classes represent discretised
637 interpretations of the underlying continuum.

638 Depth-resolved behaviour further supported this interpretation. A systematic vertical organisation of
639 texture classes emerged across class domain, with finer textures preferentially expressed at depth and
640 coarser or loamy textures concentrated near the surface (Figure 4). The C, SiC, and SC classes exhibited
641 signs of illuviation around 60 cm and remained stable through the remainder of the profile, whereas SiL

642 and SL followed the opposite trend. Nevertheless, these overall patterns aligned with established
643 pedological processes such as eluviation–illuviation, residual enrichment, and cumulative weathering
644 (Buol et al., 2011; Jenny, 1941). These trends were recovered without explicit depth stratification or
645 class-specific constraints. Mutual information remained high and independent of depth, exceeding 0.99
646 across all harmonised intervals, indicating strong class fidelity, while C-SoftG exhibited decreasing
647 values with depth, suggesting reduced structural coherence in deeper horizons.

648 Uncertainty was not associated with depth-related class behavior; it neither tracked class-specific depth
649 trends nor displayed an independent, quantifiable trend with depth. However, they were also independent
650 of number of observations, making it challenging to interpret and seemingly decoupled from the system.
651 However, these uncertainty estimates provide useful contextual information within the harmonised
652 dataset. For example, the Si class exhibited relatively more and consistent uncertainty at the global scale
653 than any other classes, or we can be 60% certain that the interpolations are Si from 15 – 60 cm. This is
654 also where SL and LS, the neighboring classes start to decline and where Si reaches its uncertainty plateau.

655 This structure arises from the physics-informed, energy-minimising formulation of phySpline (Table 6).
656 From top to bottom, energy gradually declines with depth, reflecting measurable structural variability.
657 Given the model’s numerous constraints and limited degrees of freedom, the absolute energy is expected
658 to exceed that of reference groups. Cumulative mass weighting progressively stiffens the spline with
659 depth, allowing greater variability and thus higher energy near the surface while suppressing unrealistic
660 oscillations in deeper horizons, a limitation previously noted for equal-area splines below discrete
661 transitions (Odgers et al., 2012). The depth-resolved behavior reconstructed by phySpline aligns with
662 classical pedological concepts: horizon boundaries act as conceptual thresholds rather than abrupt
663 physical breaks (Schaetzl and Thompson, 2015). By preserving continuous gradients and minimising
664 rather than eliminating energy, phySpline retains information lost in purely geometric approaches (e.g.,
665 C-EAS) and accurately represents the vertical integration of pedogenic processes.

666 At the global scale, phySpline demonstrates strong generalization, as evidenced by the consistent overall
667 trend, decoupled uncertainties, and the energy-minimising regularisation term. These features indicate
668 that the method reliably captures soil structural patterns while preserving physically meaningful gradients
669 across diverse landscapes.

670 4.2.4 Provincial scale: spatial heterogeneity and profile coherence

671 Spatial analysis along with transect views of the phySplines were incorporated into the province scale
672 analysis. Spatial classification accuracy ranged from approximately 50 to 54% across depth intervals,
673 which was considered sufficient to support profile-level interpretation as it was consistent to other studies
674 (Chaney et al., 2016; Radočaj et al., 2023; Sabbaghi et al., 2024) for depth-function-based soil mapping
675 using national and continental scale maps (Bodenstein et al., 2022; Feeney et al., 2022; Simperegui et
676 al., 2025) with the high degree of vertical accuracy 96%.

677 The spatial prediction served primarily as a vehicle for assessing profile-scale behaviour across
678 contrasting landscapes (Figure 5) and the transects show the lateral view (Figure 6). The predicted maps
679 reflect various soil-forming processes across the province, ranging from aeolian deposits with deep S
680 enriched Psamments (Kandosols) and Calcids (Calcarasols) in the west supporting livestock. Deep C rich
681 Vertisols follow mafic/ultra-mafic parent material and the saline basins of the Murry-Darling Basin
682 network (Gray et al., 2016). Illuviation occurs with C accumulation around 30 to 60 cm on the stable
683 rolling hills of the western slopes in highly fertile Alfisols (Chromosols) supporting various crops (Scott
684 et al., 2007). The progression continues into the high-energy erosional regimes of the Eastern Highlands,
685 which are characterised by fluctuating soil states and types, and finally to the dynamic alluvial deposition
686 of the floodplains (Pain et al., 2011; Searle, 2021).

687 The transect visualisations are a great tool for environmental models with their essential movement from
688 the academic to the public domain where clear communication and visualisation are critical (Dahlstrom,

689 2014; Pandey et al., 2014; Vereecken et al., 2016). Smooth, laterally coherent depth transitions were
690 maintained across both transects despite strong contrasts in visualisation techniques, soil type and
691 landscape position. The transects reflect what was seen in the two-dimensional maps and help visualise
692 the more realistic multi-dimensional state of soil where three-dimensional soil mapping is becoming
693 more important (Lin et al., 2025). Therefore, with this knowledge and visualisation method, it becomes
694 viable not only to interpolate unseen classes but also to predict and visualise unseen profiles based on
695 soil types or geomorphic patterns using the framework from Wiese et al. (2016).

696 Despite pronounced class imbalance, dominant textures such as C remained stable and were
697 underpredicted by less than 1% (Table 7), while low-prevalence classes such as SiC, SiCL and SiL were
698 overpredicted by small margins of 0.67% or less. Misclassifications occurred systematically among
699 adjacent texture classes, reflecting transitional uncertainty rather than failure to capture dominant textures
700 and was not a result of class numbers. Class-resolved structural diagnostics corroborated these findings
701 (Figure 7). Integrated process scores remained low across all texture classes (0.20–0.77), with
702 contributions dominated by internal curvature rather than boundary mismatches or boundary
703 discontinuities. Transitional textures exhibited slightly higher internal energy, consistent with their
704 pedological role as intermediate textures rather than discrete endmembers. This indicates that the model
705 complexity is concentrated on resolving the fluid gradients between these textural poles rather than
706 correcting for mathematical inconsistencies at the horizon interfaces.

707 The province scale showed the visualisation power of classification and the predictions closely followed
708 the spatial patterns of NSW lithology maps (Gray et al., 2016) and Australian soil classification map
709 (Malone et al., 2025). While this correspondence is expected due to shared environmental covariates,
710 phySpline reproduces these patterns through a physics-informed framework, rather than explicit spatial
711 tuning. This suggests that spatial soil class predictions can be interpreted as expressions of underlying

712 potential energy gradients and self-regularisation of Euler's cumulative mass process, an implication that
713 warrants further investigation.

714 4.2.5 Local scale: linking spline behaviour to pedogenetic processes

715 At the local scale, the phySpline facilitated direct interpretation of soil-forming processes by integrating
716 depth-continuous predictions with environmental covariates. The Neno District dataset included 65 soil
717 profiles with well-represented soil texture classes, from which six profiles were selected for detailed
718 analysis across a range of slopes, elevations, precipitation regimes and landform elements (Figure 8;
719 Figure 2). Selected profiles varied in depth from 35 to 180 cm and encompassed shallow, coarse-textured
720 soil (LS-SL) to a deep, fine-textured soil (SC-C).

721 In many profiles, additional interpolated texture classes emerged (11 classes) relative to the original
722 observations (7 classes), reflecting the spline's ability to resolve transitional states that are typically
723 unobserved yet pedologically plausible. This highlights the complexity of categorical transitions often
724 overlooked by conventional models and demonstrates that these transitions can be captured
725 deterministically and analytically, without relying on fuzzy-set approaches. Most profiles exhibited
726 systematic enrichment in finer particles with depth, consistent with percolation-driven clay translocation
727 processes such as lessivage.

728 Different topography, precipitation, temperature and slope position all reflect the differences in the
729 profiles seen (Table 8). Nevertheless, it was thought that geology, vegetation and time were the main
730 environmental factors contributing to the pattern of soil patterns seen, factors that are more difficult to
731 examine due to timescales and dynamics. In the Neno mountain region, stabilising vegetation enhanced
732 water infiltration and reduced surface runoff, thus promoting clay accumulation in the upper subsoil,
733 consistent with previous findings on soil–vegetation interactions on mafic substrates (De Baets et al.,
734 2006; Gyssels et al., 2005).

735 Particularly in profiles C and F, these were interpretable in terms of lateral water movement and
736 landscape position rather than vertical drainage, both showing a pronounced clay increase around 10–15
737 cm. This reflects downslope translocation of clay influenced by steep slopes (>9%), where erosion has
738 depleted the topsoil, exposing the clay-rich subsoil. Profile E was found in a similar location but with a
739 slope of 16%, and it was inferred that erosion had completely removed the topsoil. Profiles A, B, and D
740 are located in the Lisungwe Valley on sloping positions with light textures (LS–SL), where water moves
741 predominantly vertically on spur, slope, and hollow positions. Profile D is deeper, most likely due to the
742 accumulation potential of hollows, as it is a concave slope, unlike a spur, which is a convex slope.

743 Profiles A, B and D overshot their endmember classes; however, this occurred in a mass-conservative
744 manner and resulted in representations that were more pedologically realistic than solutions constrained
745 to remain strictly within class bounds. Profiles C and F did not overshoot their endmembers and were
746 initially consistent with expected pedological structure. However, Profile F required the center of mass
747 to be shifted toward the top of the horizon to achieve a more realistic representation.

748 These observations are particularly important for depth harmonisation, as they demonstrate that
749 uncertainty patterns were largely decoupled from continuous interpolations. This indicates that the
750 imposed boundary constraints maintained numerical stability and continuity, while mitigating limitations
751 previously associated with drift effects. The partial independence between uncertainty estimates and
752 interpolated class assignments gives phySpline distinct practical and conceptual utility. Whereas high
753 uncertainty is often interpreted as misclassification or insufficient sample support, in phySpline
754 uncertainty is directly proportional to proximity to a class transition. In the Neno District, classifications
755 were largely correct, and elevated uncertainties consistently reflected transitional states rather than model
756 failure, indicating a measure that can be meaningfully used in practice without complexity.

757 4.2.6 Transferability, data requirements and limitations

758 The consistent performance of phySpline across global, provincial, and local scales demonstrates its
759 robustness and transferability beyond the regions explicitly evaluated. Unlike purely data-driven
760 classifiers, phySplines are governed by the information by self-regularisation and minimising the
761 potential energy, making predictions independent of spatial support or sample size. Consequently,
762 variations in observation density do not compromise structural integrity or class transitions. Comparable
763 accuracy, class balance, and process-based diagnostics were observed in both sparsely sampled regions
764 (e.g., NSW) and densely sampled regions (e.g., Neno), despite differences in sampling density, landscape
765 heterogeneity, and soil moisture regimes.

766 At minimum, phySplines require vertically ordered soil horizon observations with defined depth intervals
767 and categorical texture assignments. The method tolerates missing horizons through controlled
768 extrapolation, but at least two observed horizons are required to anchor the latent process curve. Each
769 profile is solved independently, so performance is driven by the number and quality of profiles rather
770 than spatial sampling density. Where not all texture classes are observed, phySplines can be informed
771 that additional classes are permissible, allowing transitional classes to emerge naturally along the latent
772 curve. Where latent ordering is not apparent (e.g., numerical classification) can be arranged according to
773 physically meaningful attributes, such as diagnostic horizon moisture, drainage class or Munsell color.
774 Importantly, unlike over-constrained spline formulations (e.g., C-EAS), phySplines do not become over-
775 constrained, meaning additional constraints can be applied without compromising the solution.

776 Performance may degrade when profiles are extremely shallow and abrupt horizons, lack reliable vertical
777 ordering or include inconsistently defined texture classes across surveys. Limitations inherent to
778 taxonomic classification may influence spline performance. In soil science, C, Si and S are commonly
779 measured and combined to define texture classes. Except for C, neither S nor Si represent dominant

780 classes or display systematic depth-dependent transitions at any scale, reflecting their limited influence
781 on profile structure. This may arise from the specific USDA diagnostic dimensions used ($S = 0.05\text{--}2.0$
782 mm; $Si = 0.002\text{--}0.05$ mm) or from the GlobalSoilMap standard depth intervals. Prior studies have
783 similarly noted that conventional taxonomic systems may be unable to fully capture their functional roles
784 (Duniway et al., 2013; Hartemink, 2015; Morrow, 2023; Vigués Jorba et al., 2025). Consequently, the
785 depth intervals may have either highlighted this limitation, contributed to its manifestation in the dataset
786 or the soil texture classification did.

787 Future improvements could incorporate probabilistic uncertainty via Bayesian or Monte Carlo methods.
788 While current deterministic interpolations are easily interpretable and support endmember
789 reconstruction, probabilistic approaches could enhance risk assessment or climate-change modeling.
790 Although the algorithm is computationally efficient (~101,568 profiles in <9 min), large raster datasets
791 will require further optimisation, such as parallelisation or implementation on platforms like Google
792 Earth Engine, building on recent advances in grid-based (Flynn et al., 2024). The phySpline framework
793 could be extended to a multinomial or multi-dimensional latent space, allowing it to capture complex
794 inter-class transitions while remaining physics-informed and interpretable, though adoption depends on
795 acceptance of this multidimensional perspective.

796 4.2.7 Implications for taxonomic information and pedometrics

797 In practice, phySplines transform what was once a computational and conceptual bottleneck into a fully
798 continuous, analytically tractable framework. By resolving chronic profile boundary instabilities and
799 complex categorical transitions found in traditional splines, they maintain pedological realism through a
800 system that is mass-conservative, energy minimising, self-regularising and analytically solvable. Their
801 ability to handle class imbalances and remain transferable across diverse sampling densities opens the
802 way for next-generation soil profile modelling. Ultimately, phySplines demonstrate that the complex

803 transitions inherent to pedological philosophy hold untapped potential for soil thermodynamic
804 multifunctionality; by quantifying these gradients, the framework converts static taxonomic observations
805 into a dynamic, interpretable story of the vertical soil continuum. This provides researchers,
806 policymakers and environmental models with a framework to meaningfully visualise and understand soil
807 complexity.

808 PhySplines employ the exact analytic integral of the Euler cumulative resistance process, which
809 integrates stiffness continuously across the full horizon thickness. This shift eliminates the "midpoint
810 trap," ensuring that both boundary and interior behaviour are informed by the actual distribution of
811 mechanical and structural resistance. By capturing the continuous cumulative effect of depth-dependent
812 stiffness, the method preserves physically consistent curvature, maintains exact horizon continuity and
813 allows boundary conditions to emerge naturally. The result is a fully physics-informed, analytically
814 tractable spline that represents the horizon as a continuous process rather than a discrete approximation,
815 providing a realistic profile view that is not over-constrained.

816 Crucially, this framework bridges the gap between taxonomic nomenclature and physical laws:
817 categorical shifts are treated as high-fidelity indicators of pedogenetic change. Traditional, over-
818 constrained numerical splines are replaced with a physics-informed, flexible system that respects both
819 soil processes and mathematical rigour. This approach captures complex landscape trends within a
820 deterministic framework, mimicking the experience of traversing a terrain where environmental
821 gradients blend seamlessly into distinct soil classes. By resolving previously unmodelled transitions,
822 phySplines preserve taxonomic fidelity without sacrificing mathematical precision, offering a visually
823 accurate and interpretable way to "see" between horizons.

824 Conclusion

825 This study introduced phySpline, a physics informed, analytically solvable spline for interpolating
826 categorical soil classes across depth. By embedding pedological philosophy including continuity whether
827 gradual or virtually discrete and horizon boundary constraints into a fully continuous and differentiable
828 framework, phySpline captures both observed and previously unmodeled transitional states, preserving
829 process-based gradients that reflect real soil processes. Across global, provincial and local scales,
830 phySpline achieved high classification accuracy while maintaining mass preservation, potential energy
831 minimisation and pedological fidelity within a deterministic model. By bridging soil texture classes and
832 exact integrals, phySpline maintains interpretability and supports effective communication within a
833 mathematically robust framework. By resolving complex transitions and anchoring profile terminals,
834 phySpline transforms discrete, human-assigned classes into continuous, physically meaningful
835 representations. Future applications should extend this framework to multinomial and continuous
836 properties, establishing a multifunctional platform that integrates physics-informed constraints with data-
837 driven modeling to advance a new paradigm for profile-level soil interpolations and multi-disciplinary
838 interpretations.

839 References

840 Amundson, R., Sanderman, J., Yoo, K., Chitsaz, M., Abramova, A., Georgiou, K., 2025. Neglecting
841 vertical transport leads to underestimated soil carbon dynamics. *Nat. Geosci.* 18, 1239–1244.
842 <https://doi.org/10.1038/s41561-025-01846-6>

843 Araya, Y.N., Emmott, A., Rawes, W., Zuza, E.J., 2023. Promoting climate-smart sustainable agroforestry
844 to tackle social and environmental challenges: The case of macadamia agroforestry in Malawi.
845 *Journal of Agriculture and Food Research* 14, 100846–100846.
846 <https://doi.org/10.1016/j.jafr.2023.100846>

847 ASRIS, 2024. ASRIS - Australian Soil Resource Information System.

848 Australian Bureau Of Meteorology, 2019. Australian Gridded Climate Data (AGCD).

849 Basu, S., Isik, M.U., 2020. Categorical Complexity. Forum of Mathematics, Sigma.

850 <https://doi.org/10.48550/ARXIV.1610.07737>

851 Benbi, D.K., Toor, A.S., 2026. Spatial and Depth Distribution of Soil Carbon and Nitrogen in Relation

852 to Agricultural Management, Climate and Textural Control on Carbon Sequestration Potential.

853 Communications in Soil Science and Plant Analysis 57, 248–267.

854 <https://doi.org/10.1080/00103624.2025.2589768>

855 Bishop, T.F.A., McBratney, A.B., Laslett, G.M., 1999. Modeling soil attribute depth functions with equal-

856 area quadratic smoothing splines. Geoderma 91, 27–45. [https://doi.org/10.1016/S0016-7061\(99\)00003-8](https://doi.org/10.1016/S0016-7061(99)00003-8)

857

858 Blewett, Richard (Ed.), 2012. Shaping a Nation: A Geology of Australia. ANU Press.

859 <https://doi.org/10.22459/SN.08.2012>

860 Bodenstein, D., Clarke, C., Watson, A., Miller, J., Van Der Westhuizen, S., Rozanov, A., 2022. Evaluation

861 of global and continental scale soil maps for southern Africa using selected soil properties.

862 CATENA 216, 106381. <https://doi.org/10.1016/j.catena.2022.106381>

863 Bortolus, A., 2008. Error Cascades in the Biological Sciences: The Unwanted Consequences of Using

864 Bad Taxonomy in Ecology. AMBIO: A Journal of the Human Environment 37, 114–118.

865 [https://doi.org/10.1579/0044-7447\(2008\)37%255B114:ECITBS%255D2.0.CO;2](https://doi.org/10.1579/0044-7447(2008)37%255B114:ECITBS%255D2.0.CO;2)

866 Buol, S.W., Southard, R.J., Graham, R.C., McDaniel, P.A., 2011. Soil Genesis and Classification, 1st ed.

867 Wiley. <https://doi.org/10.1002/9780470960622>

868 Burrough, P.A., Van Gaans, P.F.M., Hootsmans, R., 1997. Continuous classification in soil survey: Spatial

869 correlation, confusion and boundaries. Geoderma 77, 115–135. [https://doi.org/10.1016/S0016-7061\(97\)00018-9](https://doi.org/10.1016/S0016-7061(97)00018-9)

870

871 Chaney, N.W., Wood, E.F., McBratney, A.B., Hempel, J.W., Nauman, T.W., Brungard, C.W., Odgers,
872 N.P., 2016. POLARIS: A 30-meter probabilistic soil series map of the contiguous United States.
873 *Geoderma* 274, 54–67. <https://doi.org/10.1016/j.geoderma.2016.03.025>

874 Cheng, C., Messerschmidt, L., Bravo, I., Waldbauer, M., Bhavikatti, R., Schenk, C., Grujic, V., Model,
875 T., Kubinec, R., Barceló, J., 2024. A General Primer for Data Harmonization. *Sci Data* 11, 152.
876 <https://doi.org/10.1038/s41597-024-02956-3>

877 Cohen, J., 1960. A Coefficient of Agreement for Nominal Scales. *Educational and Psychological
878 Measurement* 20, 37–46. <https://doi.org/10.1177/001316446002000104>

879 Colwell, J.D., 1970. A statistical-chemical characterization of four great soil groups in Southern New
880 South Wales based on orthogonal polynomials. *Soil Research* 8, 221–238.

881 CSIRO, 2024. Australian Soil Resource Information System Website. Data Collection.

882 Dahlstrom, M.F., 2014. Using narratives and storytelling to communicate science with nonexpert
883 audiences. *Proc. Natl. Acad. Sci. U.S.A.* 111, 13614–13620.
884 <https://doi.org/10.1073/pnas.1320645111>

885 De Baets, S., Poesen, J., Gyssels, G., Knapen, A., 2006. Effects of grass roots on the erodibility of topsoils
886 during concentrated flow. *Geomorphology* 76, 54–67.
887 <https://doi.org/10.1016/j.geomorph.2005.10.002>

888 Duniway, M.C., Miller, M.E., Brown, J., Toeves, G., 2013. An alternative to soil taxonomy for describing
889 key soil characteristics. *Frontiers in Ecol. & Environ.* 11, 527–528.
890 <https://doi.org/10.1890/13.WB.020>

891 Feeney, C.J., Cosby, B.J., Robinson, D.A., Thomas, A., Emmett, B.A., Henrys, P., 2022. Multiple soil
892 map comparison highlights challenges for predicting topsoil organic carbon concentration at
893 national scale. *Sci Rep* 12, 1379. <https://doi.org/10.1038/s41598-022-05476-5>

894 Fick, S.E., Hijmans, R.J., 2017. WorldClim 2: new 1km spatial resolution climate surface for global land
895 areas. *International Journal of Climatology* 37, 4302–4315.

896 Flynn, T., de Clercq, W., Rozanov, A., Clarke, C., 2019. High-resolution digital soil mapping of multiple
897 soil properties: an alternative to the traditional field survey? *South African Journal of Plant and*
898 *Soil* 1–11. <https://doi.org/10.1080/02571862.2019.1570566>

899 Flynn, T., Kostecki, R., Rebi, A., Raza, T., 2024. Accessing global soil raster images and equal-area
900 splines to estimate soil organic carbon stocks on the regional scale. *Pedosphere*
901 S1002016024000699. <https://doi.org/10.1016/j.pedsph.2024.07.004>

902 Flynn, T., Rozanov, A., Ellis, F., de Clercq, W., Clarke, C., 2022a. Farm-scale digital soil mapping of soil
903 classes in South Africa. *South African Journal of Plant and Soil*.
904 <https://doi.org/10.1080/02571862.2022.2059115>

905 Flynn, T., Wiese, L., Rozanov, A., 2022b. Soil carbon stock assessment using depth and spatial models
906 on afforested arable lands. *South African Journal of Plant and Soil* 1–13.
907 <https://doi.org/10.1080/02571862.2022.2079741>

908 Gray, J.M., Bishop, T.F.A., Wilford, J.R., 2016. Lithology and soil relationships for soil modelling and
909 mapping. *CATENA* 147, 429–440. <https://doi.org/10.1016/j.catena.2016.07.045>

910 Gyssels, G., Poesen, J., Bochet, E., Li, Y., 2005. Impact of plant roots on the resistance of soils to erosion
911 by water: a review. *Progress in Physical Geography: Earth and Environment* 29, 189–217.
912 <https://doi.org/10.1191/0309133305pp443ra>

913 Hartemink, A.E., 2015. The use of soil classification in journal papers between 1975 and 2014. *Geoderma*
914 *Regional* 5, 127–139. <https://doi.org/10.1016/j.geodrs.2015.05.002>

915 Hastie, T., Tibshirani, R., Friedman, J., 2009. *The Elements of Statistical Learning*, 2nd ed. Springer
916 Series in Statistics.

917 Henderson, M.M., Serences, J.T., Rungratsameetaweemana, N., 2025. Dynamic categorization rules alter
918 representations in human visual cortex. *Nat Commun* 16, 3459. <https://doi.org/10.1038/s41467-025-58707-4>

920 Hillebrand, H., Blasius, B., Borer, E.T., Chase, J.M., Downing, J.A., Eriksson, B.K., Filstrup, C.T.,
921 Harpole, W.S., Hodapp, D., Larsen, S., Lewandowska, A.M., Seabloom, E.W., Van De Waal,
922 D.B., Ryabov, A.B., 2018. Biodiversity change is uncoupled from species richness trends:
923 Consequences for conservation and monitoring. *Journal of Applied Ecology* 55, 169–184.
924 <https://doi.org/10.1111/1365-2664.12959>

925 Hillel, D., 1998. Environmental Soil Physics, *Journal of Environment Quality*. Academic Press, San
926 Diego, CA. <https://doi.org/10.2134/jeq1999.00472425002800060046x>

927 Isaac, N., 2004. Taxonomic inflation: its influence on macroecology and conservation. *Trends in Ecology
928 & Evolution* 19, 464–469. <https://doi.org/10.1016/j.tree.2004.06.004>

929 ISRIC, 2021. World Soil Information Service (WoSIS). ISRIC - World Soil Information.

930 Jenny, H., 1941. Factors of Soil Formation: A System of Quantitative Pedology. McGraw- Hill, NY.
931 <https://doi.org/10.2307/211491>

932 Kempen, B., Brus, D.J., Stoorvogel, J.J., 2011. Three-dimensional mapping of soil organic matter content
933 using soil type-specific depth functions. *Geoderma* 162, 107–123.

934 Kienast-Brown, S., Philippe, J., Nauman, T., Libohova, Z., Roecker, S., Thompson, J., 2021. Comparison
935 of Spline Depth Interval and Point-Depth Approaches for Predicting Soil Properties. Presented at
936 the 2021 NCSS (National Cooperative Soil Survey) National Conference., USDA-NRCS.

937 Kleidon, A., 2010. Life, hierarchy, and the thermodynamic machinery of planet Earth. *Physics of Life
938 Reviews* 7, 424–460. <https://doi.org/10.1016/j.plrev.2010.10.002>

939 Kuhn, M., Johnson, K., 2013. Applied Predictive Modeling. Springer New York.
940 <https://doi.org/10.1007/978-1-4614-6849-3>

941 Leewis, M.-C., Lawrence, C.R., Schulz, M.S., Tfaily, M.M., Ayala-Ortiz, C.O., Flores, G.E.,
942 Mackelprang, R., McFarland, J.W., 2022. The influence of soil development on the depth
943 distribution and structure of soil microbial communities. *Soil Biology and Biochemistry* 174,
944 108808. <https://doi.org/10.1016/j.soilbio.2022.108808>

945 Lin, Z., Xu, J., Lu, M., 2025. Enhanced three-dimensional mapping of soil texture components using
946 quantile regression forest and spline techniques in Jiangsu Province, China. *Sci Rep* 16, 1646.
947 <https://doi.org/10.1038/s41598-025-31144-5>

948 Ma, Y., Condon, L.E., Koch, J., Bennett, A., Defnet, A., Tijerina-Kreuzer, D., Melchior, P., Maxwell,
949 R.M., 2026. High resolution US water table depth estimates reveal quantity of accessible
950 groundwater. *Commun Earth Environ* 7, 45. <https://doi.org/10.1038/s43247-025-03094-3>

951 Malone, B., Searle, R., 2022. Soil and Landscape Grid National Soil Attribute Maps - Sand (3"
952 resolution) - Release 2. <https://doi.org/10.25919/RJMY-PA10>

953 Malone, B.P., McBratney, A.B., Minasny, B., Laslett, G.M., 2009. Mapping continuous depth functions
954 of soil carbon storage and available water capacity. *Geoderma* 154, 138–152.
955 <https://doi.org/10.1016/j.geoderma.2009.10.007>

956 Malone, B.P., Searle, R., Stenson, M., McJannet, D., Zund, P., Román Dobarco, M., Wadoux, A.M.J.-C.,
957 Minasny, B., McBratney, A., Grundy, M., 2025. Update and expansion of the soil and landscape
958 grid of Australia. *Geoderma* 455, 117226. <https://doi.org/10.1016/j.geoderma.2025.117226>

959 McDougall, K.L., Hardy, G.E.S.J., Hobbs, R.J., 2002. Distribution of *Phytophthora cinnamomi* in the
960 northern jarrah (*Eucalyptus marginata*) forest of Western Australia in relation to dieback age and
961 topography. *Australian Journal of Botany* 50, 107–107. <https://doi.org/10.1071/BT01040>

962 Morrow, K.H., 2023. A Scale Problem with the Ecosystem Services Argument for Protecting
963 Biodiversity. *Environmental Values* 32, 271–290.
964 <https://doi.org/10.3197/096327122X16569260361751>

965 NSW Department of Primary Industries, 2020. Agricultural production in New South Wales: Crop
966 statistics. NSW Government.

967 Odgers, N.P., Libohova, Z., Thompson, J.A., 2012. Equal-area spline functions applied to a legacy soil
968 database to create weighted-means maps of soil organic carbon at a continental scale. *Geoderma*
969 189–190, 153–163. <https://doi.org/10.1016/j.geoderma.2012.05.026>

970 Odom, W., Doctor, D., 2023. Rapid estimation of minimum depth-to-bedrock from lidar leveraging deep-
971 learning-derived surficial material maps. *Applied Computing and Geosciences* 18, 100116.
972 <https://doi.org/10.1016/j.acags.2023.100116>

973 Pain, C., Gregory, L., Wilson, P., McKenzie, N., 2011. Physiographic Regions of Australia.
974 <https://doi.org/10.25919/52XM-CH28>

975 Pandey, A.V., Manivannan, A., Nov, O., Satterthwaite, M., Bertini, E., 2014. The Persuasive Power of
976 Data Visualization. *IEEE Trans. Visual. Comput. Graphics* 20, 2211–2220.
977 <https://doi.org/10.1109/TVCG.2014.2346419>

978 Pei, J., Li, J., Luo, Y., Rillig, M.C., Smith, P., Gao, W., Li, B., Fang, C., Nie, M., 2025. Patterns and
979 drivers of soil microbial carbon use efficiency across soil depths in forest ecosystems. *Nat
980 Commun* 16, 5218. <https://doi.org/10.1038/s41467-025-60594-8>

981 Ponce-Hernandez, R., Marriott, F.H.C., Beckett, P.H.T., 1986. An improved method for reconstructing a
982 soil profile from analyses of a small number of samples. *Journal of Soil Science* 37, 455–467.

983 Probst, A.J., Ladd, B., Jarett, J.K., Geller-McGrath, D.E., Sieber, C.M.K., Emerson, J.B., Anantharaman,
984 K., Thomas, B.C., Malmstrom, R.R., Stieglmeier, M., Klingl, A., Woyke, T., Ryan, M.C.,
985 Banfield, J.F., 2018. Differential depth distribution of microbial function and putative symbionts
986 through sediment-hosted aquifers in the deep terrestrial subsurface. *Nat Microbiol* 3, 328–336.
987 <https://doi.org/10.1038/s41564-017-0098-y>

988 Radočaj, D., Jurišić, M., Rapčan, I., Domazetović, F., Milošević, R., Plaščak, I., 2023. An Independent
989 Validation of SoilGrids Accuracy for Soil Texture Components in Croatia. *Land* 12, 1034.
990 <https://doi.org/10.3390/land12051034>

991 Rogozovsky, I., Ansmann, A., Hofer, J., Chudnovsky, A., 2025. Unveiling Atmospheric Layers: Vertical
992 Pollution Patterns and Prospects for High-Resolution Aerosol Retrievals Using the Eastern
993 Mediterranean as a Case Study. *Environ. Sci. Technol.* 59, 12181–12195.
994 <https://doi.org/10.1021/acs.est.4c14556>

995 Ruiz, O.E., Wagenaar, J.B., Mehta, B., Ziogas, I., Swanson, L., Worley, K.C., Cruz-Almeida, Y., Johnson,
996 A.J., Boline, J., Boccanfuso, J., Martone, M.E., Haelterman, N.A., 2025. A guide to developing
997 harmonized research workflows in a team science context. *Experimental Neurology* 392, 115333.
998 <https://doi.org/10.1016/j.expneurol.2025.115333>

999 Russell, J.S., Moore, A.W., 1968. Comparison of different depth weighting in the numerical analysis of
1000 anisotropic soil profile data. Presented at the Transaction of the 9th International Congress,
1001 International Soil Science Society, Adelaide, Australia, pp. 205–213.

1002 Sabbaghi, M.A., Esfandiari, M., Eftekhari, K., Torkashvand, A.M., 2024. Predictive map of soil texture
1003 classes using decision tree model and neural network with features of geomorphology level. *Can.
1004 J. Soil. Sci.* 104, 72–90. <https://doi.org/10.1139/cjss-2023-0011>

1005 Schaetzl, R.J., Thompson, M.L., 2015. *Soils: genesis and geomorphology*, Second edition. ed. Cambridge
1006 University Press, New York, NY.

1007 Scott, B.J., Fenton, I.G., Fanning, A.G., Schumann, W.G., Castleman, L.J.C., 2007. Surface soil acidity
1008 and fertility in the eastern Riverina and Western Slopes of southern New South Wales. *Aust. J.
1009 Exp. Agric.* 47, 949. <https://doi.org/10.1071/EA05155x>

1010 Searle, R., 2021. Soil and Landscape Grid National Soil Attribute Maps - Australian Soil Classification
1011 Map (3" resolution) - Release 1. <https://doi.org/10.25919/VKJN-3013>

1012 Simperegui, K.B.D., Kouame, A.K.K., Kwasie, B., Bindraban, P.S., Adzawla, W., Asamoah, E., El
1013 Gharous, M., 2025. Digital mapping of Ghana's soil properties and nutrients: performance of
1014 spline and weighted average approaches. *Geoderma* 459.
1015 <https://doi.org/10.1016/j.geoderma.2025.117365>

1016 Smith, J.A., Robert B. Thompson, 2019. Livestock Production in New South Wales: Current Trends and
1017 Future Projections. *Australian Journal of Agricultural Science* 54, 125–140.

1018 Souza, L.F.T., Hirmas, D.R., Sullivan, P.L., Reuman, D.C., Kirk, M.F., Li, L., Ajami, H., Wen, H., Sarto,
1019 M.V.M., Loecke, T.D., Rudick, A.K., Rice, C.W., Billings, S.A., 2023. Root distributions,

1020 precipitation, and soil structure converge to govern soil organic carbon depth distributions.

1021 *Geoderma* 437, 116569. <https://doi.org/10.1016/j.geoderma.2023.116569>

1022 Vereecken, H., Schnepf, A., Hopmans, J.W., Javaux, M., Or, D., Roose, T., Vanderborght, J., Young,

1023 M.H., Amelung, W., Aitkenhead, M., Allison, S.D., Assouline, S., Baveye, P., Berli, M.,

1024 Brüggemann, N., Finke, P., Flury, M., Gaiser, T., Govers, G., Ghezzehei, T., Hallett, P., Hendricks

1025 Franssen, H.J., Heppell, J., Horn, R., Huisman, J.A., Jacques, D., Jonard, F., Kollet, S., Lafolie,

1026 F., Lamorski, K., Leitner, D., McBratney, A., Minasny, B., Montzka, C., Nowak, W., Pachepsky,

1027 Y., Padarian, J., Romano, N., Roth, K., Rothfuss, Y., Rowe, E.C., Schwen, A., Šimůnek, J., Tiktak,

1028 A., Van Dam, J., Van Der Zee, S.E.A.T.M., Vogel, H.J., Vrugt, J.A., Wöhling, T., Young, I.M.,

1029 2016. Modeling Soil Processes: Review, Key Challenges, and New Perspectives. *Vadose Zone*

1030 *Journal* 15, 1–57. <https://doi.org/10.2136/vzj2015.09.0131>

1031 Vigués Jorba, J., Scherrer, D., Duchenne, F., Zellweger, F., Gossner, M.M., Bollmann, K., 2025.

1032 Differential responses of taxonomic, functional and phylogenetic multi-taxon diversity to

1033 environmental factors in temperate forest ecosystems. *Ecological Indicators* 178, 113855.

1034 <https://doi.org/10.1016/j.ecolind.2025.113855>

1035 Viscarra Rossel, R., Chen, C., Grundy, M., Searle, R., Clifford, D., Odgers, N., Holmes, K., Griffin, T.,

1036 Liddicoat, C., Kidd, D., 2014. Soil and Landscape Grid National Soil Attribute Maps - Soil Depth

1037 (3" resolution) - Release 1. <https://doi.org/10.4225/08/546F540FE10AA>

1038 Weiskopf, S.R., Myers, B.J.E., Arce-Plata, M.I., Blanchard, J.L., Ferrier, S., Fulton, E.A., Harfoot, M.,

1039 Isbell, F., Johnson, J.A., Mori, A.S., Weng, E., HarmáCková, Z.V., Londoño-Murcia, M.C.,

1040 Miller, B.W., Pereira, L.M., Rosa, I.M.D., 2022. A Conceptual Framework to Integrate

1041 Biodiversity, Ecosystem Function, and Ecosystem Service Models. *BioScience* 72, 1062–1073.

1042 <https://doi.org/10.1093/biosci/biac074>

1043 Wiese, L., Ros, I., Rozanov, A., Boshoff, A., de Clercq, W., Seifert, T., 2016. An approach to soil carbon
1044 accounting and mapping using vertical distribution functions for known soil types. *Geoderma*
1045 263, 264–273. <https://doi.org/10.1016/j.geoderma.2015.07.012>

1046 Yanofsky, N.S., 2015. Computability and Complexity of Categorical Structures.
1047 <https://doi.org/10.48550/ARXIV.1507.05305>

1048 Zhang, J., Goodchild, M.F., 2002. Uncertainty in Geographical Information, 0 ed. CRC Press.
1049 <https://doi.org/10.1201/b12624>

1050 Zhang, X., Zhang, W.-C., Wu, W., Liu, H.-B., 2023. Horizontal and vertical variation of soil clay content
1051 and its controlling factors in China. *Science of The Total Environment* 864, 161141.
1052 <https://doi.org/10.1016/j.scitotenv.2022.161141>

1053 Zhao, S., Kvale, K.F., Zhu, L., Zettler, E.R., Egger, M., Mincer, T.J., Amaral-Zettler, L.A., Lebreton, L.,
1054 Niemann, H., Nakajima, R., Thiel, M., Bos, R.P., Galgani, L., Stubbins, A., 2025. The distribution
1055 of subsurface microplastics in the ocean. *Nature* 641, 51–61. <https://doi.org/10.1038/s41586-025-08818-1>

1056

1057